



Gliese 12 b: A Temperate Earth-sized Planet at 12 pc Ideal for Atmospheric Transmission Spectroscopy

Downloaded from: <https://research.chalmers.se>, 2024-08-02 17:51 UTC


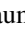
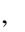
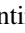
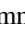




Citation for the original published paper (version of record):

Kuzuhara, M., Fukui, A., Livingston, J. et al (2024). Gliese 12 b: A Temperate Earth-sized Planet at 12 pc Ideal for Atmospheric Transmission Spectroscopy. *Astrophysical Journal Letters*, 969(1). <http://dx.doi.org/10.3847/2041-8213/ad3642>

N.B. When citing this work, cite the original published paper.



Gliese 12 b: A Temperate Earth-sized Planet at 12 pc Ideal for Atmospheric Transmission Spectroscopy

Masayuki Kuzuhara^{1,2,61} , Akihiko Fukui^{3,4,61} , John H. Livingston^{1,2,5} , José A. Caballero⁶ , Jerome P. de Leon⁷ , Teruyuki Hirano^{1,2,5} , Yui Kasagi^{1,2,5} , Felipe Murgas^{4,8} , Norio Narita^{1,3,4} , Masashi Omiya^{1,2} , Jaime Orell-Miquel^{4,8} , Enric Palle^{4,8} , Quentin Changeat^{9,10} , Emma Esparza-Borges^{4,8} , Hiroki Harakawa¹¹ , Coel Hellier¹² , Yasunori Hori^{1,2,5} , Kai Ikuta⁷ , Hiroyuki Tako Ishikawa¹³ , Takanori Kodama¹⁴ , Takayuki Kotani^{1,2,5} , Tomoyuki Kudo¹¹ , Juan C. Morales^{15,16} , Mayuko Mori⁷ , Evangelos Nagel¹⁷ , Hannu Parviainen^{4,8} , Volker Perdelwitz¹⁸ , Ansgar Reiners¹⁷ , Ignasi Ribas^{15,16} , Jorge Sanz-Forcada⁶ , Bun'ei Sato¹⁹ , Andreas Schweitzer²⁰ , Hugo M. Taberner²¹ , Takuya Takarada^{1,2} , Taichi Uyama^{22,23} , Noriharu Watanabe⁷ , Mathias Zechmeister¹⁷ , Néstor Abreu García^{4,8} , Wako Aoki^{2,5} , Charles Beichman^{23,24} , Víctor J. S. Béjar^{4,8} , Timothy D. Brandt²⁵ , Yéssica Calatayud-Borras^{4,8} , Ilaria Carleo^{4,8} , David Charbonneau²⁶ , Karen A. Collins²⁶ , Thayne Currie^{11,27} , John P. Doty²⁸ , Stefan Dreizler¹⁷ , Gareb Fernández-Rodríguez^{4,8} , Izuru Fukuda⁷ , Daniel Galán^{4,8} , Samuel Geraldía-González^{4,8} , Josafat González-Rodríguez^{4,8} , Yuya Hayashi⁷ , Christina Hedges^{29,30} , Thomas Henning³¹ , Klaus Hodapp³² , Masahiro Ikoma^{2,5} , Keisuke Isogai^{7,33} , Shane Jacobson³² , Markus Janson³⁴ , Jon M. Jenkins³⁵ , Taiki Kagetani⁷ , Eiji Kambe¹¹ , Yugo Kawai⁷ , Kiyoe Kawauchi³⁶ , Eiichiro Kokubo² , Mihoko Konishi³⁷ , Judith Korth³⁸ , Vigneshwaran Krishnamurthy^{39,40,41} , Takashi Kurokawa^{1,42} , Nobuhiko Kusakabe^{1,2} , Jungmi Kwon⁴³ , Andrés Laza-Ramos⁴⁴ , Florence Libotte^{4,8} , Rafael Luque⁴⁵ , Alberto Madrigal-Aguado^{4,8} , Yuji Matsumoto² , Dimitri Mawet^{24,46} , Michael W. McElwain²⁹ , Pedro Pablo Meni Gallardo^{4,8} , Giuseppe Morello^{4,47} , Sara Muñoz Torres^{4,8} , Jun Nishikawa^{1,2,5} , Stevanus K. Nugroho^{1,2} , Masahiro Ogihara^{48,49} , Alberto Peláez-Torres^{4,8} , David Rapetti^{35,50} , Manuel Sánchez-Benavente^{4,8} , Martin Schlecker⁵¹ , Sara Seager^{52,53,54} , Eugene Serabyn²⁴ , Takuma Serizawa^{2,42} , Monika Stangret⁵⁵ , Aoi Takahashi^{1,2} , Huan-Yu Teng^{19,56} , Motohide Tamura^{1,2,43} , Yuka Terada^{57,58} , Akitoshi Ueda^{2,5} , Tomonori Usuda^{2,5} , Roland Vanderspek⁵² , Sébastien Vievard^{1,11} , David Watanabe⁵⁹ , Joshua N. Winn⁶⁰ , and Maria Rosa Zapatero Osorio⁶

¹ Astrobiology Center, NINS, 2-21-1 Osawa, Mitaka, Tokyo 181-8588, Japan; m.kuzuhara@nao.ac.jp

² National Astronomical Observatory of Japan, NINS, 2-21-1 Osawa, Mitaka, Tokyo 181-8588, Japan

³ Komaba Institute for Science, The University of Tokyo, 3-8-1 Komaba, Meguro, Tokyo 153-8902, Japan; afukui@g.ecc.u-tokyo.ac.jp

⁴ Instituto de Astrofísica de Canarias (IAC), E-38200 La Laguna, Tenerife, Spain

⁵ Astronomical Science Program, Graduate University for Advanced Studies (SOKENDAI), 2-21-1, Osawa, Mitaka, Tokyo, 181-8588, Japan

⁶ Centro de Astrobiología, CSIC-INTA, Camino Bajo del Castillo s/n, E-28692 Villanueva de la Cañada, Madrid, Spain

⁷ Department of Multi-Disciplinary Sciences, Graduate School of Arts and Sciences, The University of Tokyo, 3-8-1 Komaba, Meguro, Tokyo 153-8902, Japan

⁸ Departamento de Astrofísica, Universidad de La Laguna (ULL), E-38206 La Laguna, Tenerife, Spain

⁹ European Space Agency (ESA), ESA Office, Space Telescope Science Institute (STScI), Baltimore, MD 21218, USA

¹⁰ Department of Physics and Astronomy, University College London, Gower Street, WC1E 6BT London, UK

¹¹ Subaru Telescope, National Astronomical Observatory of Japan, 650 North A'ohōkū Place, Hilo, HI 96720, USA

¹² Astrophysics Group, Keele University, Staffordshire, ST5 5BG, UK

¹³ Department of Physics and Astronomy, The University of Western Ontario, 1151 Richmond Street, London, ON N6A 3K7, Canada

¹⁴ Earth-Life Science Institute (ELSI), Tokyo Institute of Technology, 2-12-1-17E-315 Ookayama, Meguro-ku, Tokyo 152-8550, Japan

¹⁵ Institut de Ciències de l'Espai (ICE, CSIC), Campus UAB, Can Magrans s/n, 08193 Bellaterra, Barcelona, Spain

¹⁶ Institut d'Estudis Espacials de Catalunya (IEEC), c/ Gran Capità 2-4, 08034 Barcelona, Spain

¹⁷ Institut für Astrophysik und Geophysik, Georg-August-Universität, Friedrich-Hund-Platz 1, 37077 Göttingen, Germany

¹⁸ Department of Physics, Ariel University, Ariel 40700, Israel

¹⁹ Department of Earth and Planetary Sciences, School of Science, Tokyo Institute of Technology, 2-12-1 Ookayama, Meguro-ku, Tokyo 152-8551, Japan

²⁰ Hamburger Sternwarte, Gojenbergsweg 112, 21029 Hamburg, Germany

²¹ Departamento de Física de la Tierra y Astrofísica and IPARCOS-UCM (Instituto de Física de Partículas y del Cosmos de la UCM), Facultad de Ciencias Físicas, Universidad Complutense de Madrid, 28040, Madrid, Spain

²² Department of Physics and Astronomy, California State University Northridge, 18111 Nordhoff Street, Northridge, CA 91330, USA

²³ NASA Exoplanet Science Institute, Infrared Processing and Analysis Center, California Institute of Technology, Pasadena, CA 91125, USA

²⁴ Jet Propulsion Laboratory, California Institute of Technology, 4800 Oak Grove Drive, Pasadena, CA 91109, USA

²⁵ Department of Physics, University of California, Santa Barbara, CA, USA

²⁶ Center for Astrophysics | Harvard & Smithsonian, 60 Garden Street, Cambridge, MA 02138, USA

²⁷ Department of Physics and Astronomy, University of Texas–San Antonio, San Antonio, TX, USA

²⁸ Noqsi Aerospace Ltd., 15 Blanchard Avenue, Billerica, MA 01821, USA

²⁹ NASA Goddard Space Flight Center, Greenbelt, MD, USA

³⁰ University of Maryland, Baltimore County, 1000 Hilltop Circle, Baltimore, MD, USA

³¹ Max-Planck-Institut für Astronomie (MPIA), Königstuhl 17, 69117 Heidelberg, Germany

³² University of Hawaii, Institute for Astronomy, 640 North Aohoku Place, Hilo, HI 96720, USA

³³ Okayama Observatory, Kyoto University, 3037-5 Honjo, Kamogatacho, Asakuchi, Okayama 719-0232, Japan

³⁴ Department of Astronomy, Stockholm University, AlbaNova University Center, SE-10691, Stockholm, Sweden

³⁵ NASA Ames Research Center, Moffett Field, CA 94035, USA

³⁶ Department of Physical Sciences, Ritsumeikan University, Kusatsu, Shiga 525-8577, Japan

³⁷ Faculty of Science and Technology, Oita University, 700 Dannoharu, Oita 870-1192, Japan

³⁸ Lund Observatory, Division of Astrophysics, Department of Physics, Lund University, Box 118, 22100 Lund, Sweden

³⁹ Trotter Space Institute, McGill University, 3550 rue University, Montréal, QC H3A 2A7, Canada

⁴⁰ Department of Physics, McGill University, 3600 rue University, Montréal, QC H3A 2T8, Canada

⁴¹ Institut Trotter de Recherche sur les Exoplanètes, Université de Montréal, Montréal, QC H3T 1J4, Canada

⁴² Institute of Engineering, Tokyo University of Agriculture and Technology, 2-24-16, Nakacho, Koganei, Tokyo, 184-8588, Japan

⁴³ Department of Astronomy, Graduate School of Science, The University of Tokyo, 7-3-1, Hongo, Bunkyo-ku, Tokyo, 113-0033, Japan

⁴⁴ Departamento de Astronomía y Astrofísica, Universidad de Valencia (UV), E-46100, Burjassot, Valencia, Spain

⁴⁵ Department of Astronomy & Astrophysics, University of Chicago, Chicago, IL 60637, USA

⁴⁶ Department of Astronomy, California Institute of Technology, Pasadena, CA 91125, USA

⁴⁷ Department of Space, Earth and Environment, Chalmers University of Technology, SE-412 96 Gothenburg, Sweden

⁴⁸ Tsung-Dao Lee Institute, Shanghai Jiao Tong University, 1 Lisuo Road, Shanghai 201210, People's Republic of China

⁴⁹ School of Physics and Astronomy, Shanghai Jiao Tong University, 800 Dongchuan Road, Shanghai 200240, People's Republic of China

⁵⁰ Research Institute for Advanced Computer Science, Universities Space Research Association, Washington, DC 20024, USA

⁵¹ Steward Observatory and Department of Astronomy, The University of Arizona, Tucson, AZ 85721, USA

⁵² Department of Physics and Kavli Institute for Astrophysics and Space Research, Massachusetts Institute of Technology, 77 Massachusetts Avenue, Cambridge, MA 02139, USA

⁵³ Department of Earth, Atmospheric and Planetary Sciences, Massachusetts Institute of Technology, 77 Massachusetts Avenue, Cambridge, MA 02139, USA

⁵⁴ Department of Aeronautics and Astronautics, Massachusetts Institute of Technology, 77 Massachusetts Avenue, Cambridge, MA 02139, USA

⁵⁵ INAF-Osservatorio Astronomico di Padova, Vicolo dell'Osservatorio 5, 35122, Padova, Italy

⁵⁶ CAS Key Laboratory of Optical Astronomy, National Astronomical Observatories, Chinese Academy of Sciences, Beijing 100101, People's Republic of China

⁵⁷ Institute of Astronomy and Astrophysics, Academia Sinica, P.O. Box 23-141, Taipei 10617, Taiwan, R.O.C

⁵⁸ Department of Astrophysics, National Taiwan University, Taipei 10617, Taiwan, R.O.C

⁵⁹ Planetary Discoveries in Fredericksburg, VA 22405, USA

⁶⁰ Department of Astrophysical Sciences, Princeton University, Princeton, NJ 08544, USA

Received 2023 December 21; revised 2024 February 28; accepted 2024 March 21; published 2024 May 23

Abstract

Recent discoveries of Earth-sized planets transiting nearby M dwarfs have made it possible to characterize the atmospheres of terrestrial planets via follow-up spectroscopic observations. However, the number of such planets receiving low insolation is still small, limiting our ability to understand the diversity of the atmospheric composition and climates of temperate terrestrial planets. We report the discovery of an Earth-sized planet transiting the nearby (12 pc) inactive M3.0 dwarf Gliese 12 (TOI-6251) with an orbital period (P_{orb}) of 12.76 days. The planet, Gliese 12 b, was initially identified as a candidate with an ambiguous P_{orb} from TESS data. We confirmed the transit signal and P_{orb} using ground-based photometry with MuSCAT2 and MuSCAT3, and validated the planetary nature of the signal using high-resolution images from Gemini/NIRI and Keck/NIRC2 as well as radial velocity (RV) measurements from the InfraRed Doppler instrument on the Subaru 8.2 m telescope and from CARMENES on the CAHA 3.5 m telescope. X-ray observations with XMM-Newton showed the host star is inactive, with an X-ray-to-bolometric luminosity ratio of $\log L_X/L_{\text{bol}} \approx -5.7$. Joint analysis of the light curves and RV measurements revealed that Gliese 12 b has a radius of $0.96 \pm 0.05 R_{\oplus}$, a 3σ mass upper limit of $3.9 M_{\oplus}$, and an equilibrium temperature of 315 ± 6 K assuming zero albedo. The transmission spectroscopy metric (TSM) value of Gliese 12 b is close to the TSM values of the TRAPPIST-1 planets, adding Gliese 12 b to the small list of potentially terrestrial, temperate planets amenable to atmospheric characterization with JWST.

Unified Astronomy Thesaurus concepts: [Exoplanet astronomy \(486\)](#); [Exoplanet atmospheres \(487\)](#); [Exoplanets \(498\)](#); [Extrasolar rocky planets \(511\)](#); [Space telescopes \(1547\)](#); [Transit photometry \(1709\)](#); [Radial velocity \(1332\)](#); [Astronomy data modeling \(1859\)](#); [High resolution spectroscopy \(2096\)](#)

1. Introduction

M dwarfs are promising targets to explore terrestrial exoplanets because of their small masses and radii, which result in large reflex motions and deep transits even for small planets. In addition, the low bolometric luminosity of M dwarfs makes the habitable zone (HZ) closer to the host stars, making planets inside the HZ easier to observe compared to those inside the HZ around earlier-type stars. These advantages motivated several ground-based exoplanet-hunting projects to target nearby M dwarfs using Doppler velocimeters such as the High-accuracy Radial-velocity Planet Searcher (HARPS; Bonfils et al. 2013), the InfraRed Doppler instrument (IRD; Harakawa et al. 2022), the Calar Alto high-Resolution search for M dwarfs with Exoearths with Near-infrared and optical Echelle Spectrographs (CARMENES; Ribas et al. 2023), and

Habitable-zone Planet Finder (Mahadevan et al. 2014) and using transit photometers such as MEarth (Charbonneau et al. 2008) and SPECULOOS (Delrez et al. 2018). Nearby M dwarfs are also one of the main targets of former and ongoing space-based missions such as K2 (Howell et al. 2014) and TESS (Ricker et al. 2015).

Transiting terrestrial planets around nearby M dwarfs are of particular importance in characterizing their atmospheres, which is already feasible through transmission and/or emission spectroscopy with current facilities. So far, dozens of terrestrial-sized transiting planets have been discovered around M dwarfs within 30 pc (e.g., Gillon et al. 2017; Kreidberg et al. 2019; Crossfield et al. 2022). However, they typically orbit very close to their host stars. Their atmospheres are therefore vulnerable to the strong X-ray and ultraviolet (XUV) irradiation of their M dwarf hosts, which are known to be magnetically active in general. Indeed, recent spectroscopic emission observations of hot Earth-sized planets have refuted the existence of thick atmospheres around LHS 3844b (Kreidberg et al. 2019) and GJ 1252b (Crossfield et al. 2022), suggesting that the atmospheres (if any) of such short-period planets have difficulty surviving.

⁶¹ These two authors contributed equally to this work.



Currently, TRAPPIST-1 (Gillon et al. 2017) is the only known M dwarf within 30 pc transited by terrestrial planets with insolation of less than twice that of the Earth. Due to the proximity (12 pc) and small size ($0.12 R_{\odot}$) of the host star (Gillon et al. 2017), the seven planets orbiting TRAPPIST-1 are the best known targets for characterizing atmospheres of warm-to-cool rocky planets with Earth or sub-Earth masses. However, it is unlikely that all of the planets harbor detectable atmospheres because their orbits are all close (0.012–0.062 au; Agol et al. 2021) to the moderately active host star, whose X-ray-to-bolometric flux ratio is $\log L_X/L_{\text{bol}} \approx -3.5$ (Wheatley et al. 2017). Recent secondary eclipse observations of TRAPPIST-1 b and TRAPPIST-1 c using the MIRI instrument on board the James Webb Space Telescope (JWST) suggest that they have little to no atmosphere, though a thin atmosphere of TRAPPIST-1 c is not conclusively ruled out (Greene et al. 2023; Lincowski et al. 2023). The flat transmission spectra of the TRAPPIST-1 planets across the near-infrared wavelengths observed from the ground (Burdanov et al. 2019) and space (de Wit et al. 2016, 2018; Gressier et al. 2022) are consistent with the absence of massive atmospheres. The current list of low-insolation terrestrial planets amenable for atmospheric study is short; therefore, it is essential to expand the sample of such planets to understand the diversity of atmospheres of temperate terrestrial planets.

In this Letter, we present the discovery of a nearly Earth-sized planet with an orbital period of 12.76 days transiting the nearby (12 pc) inactive M dwarf Gliese 12. The planet is one of the best temperate⁶² Earth-sized planets amenable for transmission spectroscopy, joining the planets around TRAPPIST-1. The transit signal of this planet was first identified in the light-curve data of TESS and subsequently followed up by multiple ground-based observations.

2. TESS Observations

TESS observed Gliese 12 (TOI-6251) at 2 minutes cadence in Sectors 42, 43, 57, and 70. The observations were conducted from UT 2021 August 20 to UT 2023 October 16, resulting in photometry spanning 797 days, with gaps for data downlink in the middle of each sector and gaps of 353 and 326 days between Sectors 43–57 and 57–70, respectively. Light curves were produced by the photometry pipeline developed by Science Processing Operations Center (SPOC) at NASA Ames Research Center (Jenkins et al. 2016) using the apertures shown in Figure 1. A transit signal with a period of 12.76 days was initially detected by the SPOC using an adaptive, noise-compensating matched filter (Jenkins 2002; Jenkins et al. 2020) based on the data from Sectors 42, 43, and 57. An initial transit model including the effect of limb darkening was fitted to the signal (Li et al. 2019), and it passed a suite of diagnostic tests performed to assess its credibility (Twicken et al. 2018), including the difference image centroiding test, which located Gliese 12 within $9''.9 \pm 8''.5$ of the transit source. The TESS Science Office at Massachusetts Institute of Technology reviewed the Data Validation (DV) reports and issued an alert for this candidate planetary signal as TOI-6251.01 on UT 2023 April 3 (Guerrero et al. 2021). However, the orbital period was reported to be 25.52 days with a caution that the true orbital

⁶² We define temperate as an insolation between 4 and 0.25 times the Earth’s insolation, following Triaud et al. (2023) and TRAPPIST-1 JWST Community Initiative et al. (2023), with the caveat that it is challenging to estimate the true surface temperatures of any planets without knowing their albedo and atmospheric composition and structure.

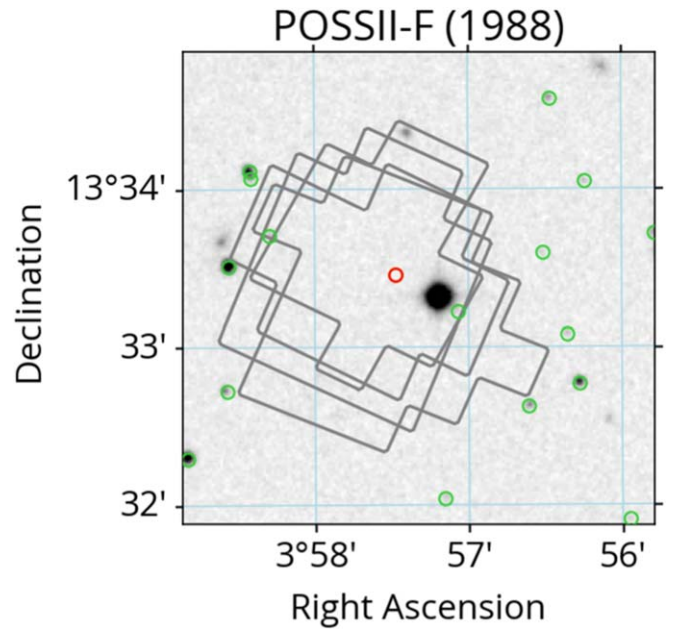


Figure 1. TESS photometric apertures from Sectors 42, 43, 57, and 70 (gray outlines) with an archival image from the POSSII-F survey taken in 1988 (Reid et al. 1991), with Gaia DR2 source positions (Gaia Collaboration et al. 2018) shown as circles; the red circle denotes the Gaia position (at epoch J2015.5) of Gliese 12, which is offset from the position in the archival image due to the star’s proper motion, and the green circles show other sources.

period may be half. This was because only one odd-numbered⁶³ transit with respect to the 12.76 day period had been observed with TESS by the time the candidate was announced, and it occurred on the edge of a data gap in Sector 57 (see Figure 2). As a result, the signal from odd-numbered transits was tentative. This motivated us to schedule follow-up photometry for odd-numbered transits using MuSCAT2 and MuSCAT3 (Section 3.2), allowing us to confirm the true orbital period to be 12.76 days (Section 4.2.2). Subsequently, TESS Sector 70 data revealed an additional odd-numbered transit that also confirmed this period. We hereafter refer to this planet candidate as Gliese 12 b (its planetary nature is validated in Section 4.4).

For the subsequent analyses in this Letter, we downloaded the Presearch Data Conditioning Simple Aperture Photometry (PDCSAP; Smith et al. 2012; Stumpe et al. 2012, 2014) light curves of all available TESS sectors from the Mikulski Archive for Space Telescopes at the Space Telescope Science Institute, which are shown in Figure 2.

3. Follow-up Observations

This section provides the details of ground-based observations to validate the planetary nature of the transit signal identified by TESS. The ground-based observations include adaptive optics (AO) imaging performed with Altair/NIRI and PyWFS/NIRC2 (Section 3.1), multiband photometry with MuSCAT2 and MuSCAT3 (Narita et al. 2019, 2020; Section 3.2), and radial velocity (RV) measurements with IRD and CARMENES (Section 3.3). We used data obtained by the IRD Strategic Survey Program of the Subaru Telescope (IRD-SSP), which independently selected Gliese 12 as one of more than 100 M-type

⁶³ The transit number is counted such that the first transit event observed in the TESS data, namely Sector 43, is zero.

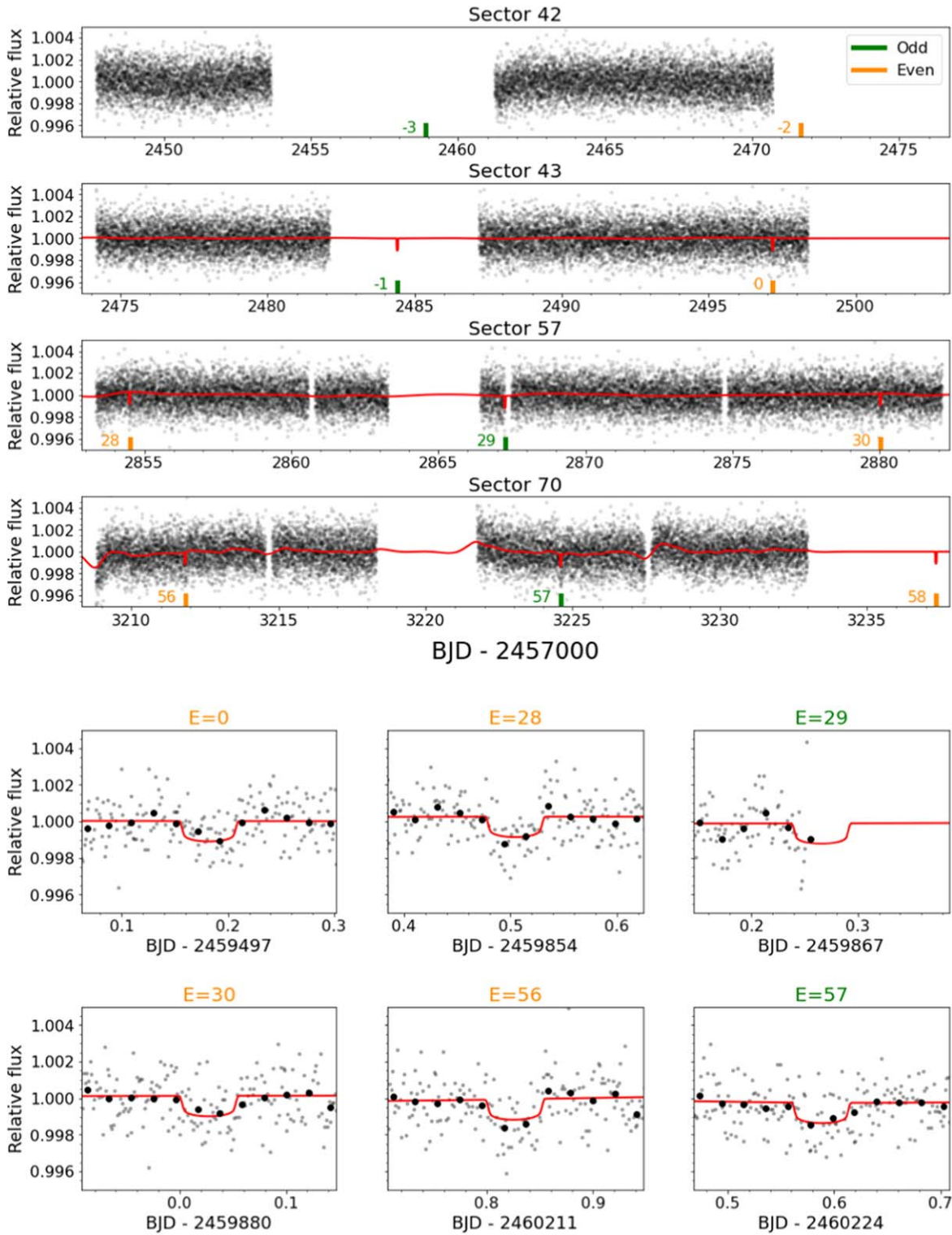


Figure 2. (First–fourth rows) TESS PDCSAP light curves of Gliese 12 from Sectors 42, 43, 57, and 70, respectively. The locations of the predicted transits assuming $P = 12.76$ days are marked by vertical bars, where green and orange indicate odd- and even-numbered transits, respectively. The relative transit epochs are labeled beside the bars. The red solid lines shown in the second–fourth panels are the light curves predicted by the maximum-likelihood transit+GP model. (Bottom two rows) Same as above, but the data around each of the six transits covered by TESS are zoomed in. The transit epochs are shown on top of each panel. The gray dots and black circles are the unbinned and 30 minute binned data, respectively. The error bars of the binned data are shown, but they are smaller than the markers.

dwarfs to search for exoplanets using the RV technique (Harakawa et al. 2022). Although the RV signal of Gliese 12 b is too small to be detected by the IRD data alone, the RV measurements from IRD are used to rule out false-positive (FP)

scenarios for the transit signal detected by TESS and constrain the presence of additional planets (Section 4.6). These data, combined with the RV data from CARMENES, enable us to place an upper limit on the mass of Gliese 12 b (Section 4.5).

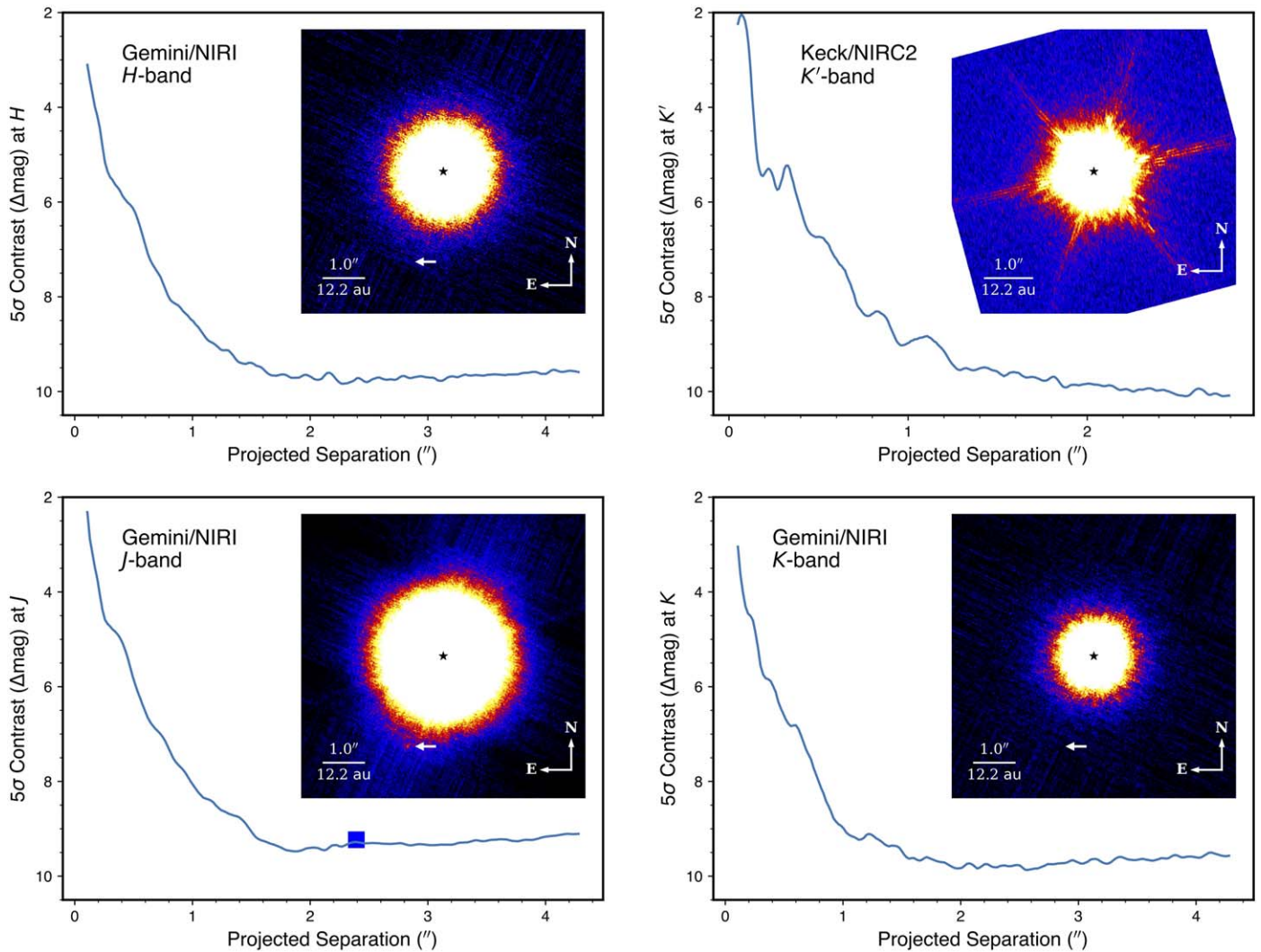


Figure 3. 5σ contrast limits at J (bottom left), H (top left), and K (bottom right) from Gemini/NIRI and at K' from Keck II/NIRC2 (top right). The combined images are shown in the insets of the panels, where Gliese 12 is at the star symbols. The maximum values of the image dynamic range were set to be 20 times higher than the noise levels at the edge areas. The locations corresponding to the identified possible source that was detected only in the J -band image are marked by arrow symbols and its contrast by a square symbol. Note that the source detection and contrast measurement were performed with the images after PSF subtractions.

3.1. AO Imaging

Gliese 12 was observed with the NIRI imager of the Gemini-North telescope (Hodapp et al. 2003) with the AO instrument Altair (Herriot et al. 2000) in the program GN-2009B-Q-10-213 (PI: S. Dieterich). The observations were conducted on UT 2009 September 18 using the near-infrared band filters at J ($\approx 1.2 \mu\text{m}$), H ($\approx 1.6 \mu\text{m}$), and K ($\approx 2.2 \mu\text{m}$). We reduced the Gemini/NIRI data downloaded from the Gemini data archive. The images after the data processing are shown in Figure 3 with the 5σ contrast curves at J , H , and K . See Appendix A for details about the observations and data reduction. As shown in Figure 3, we found that there is a possible faint source only in the J -band image, which is located at a projected separation of $\approx 2''.4$ from Gliese 12.

We derived contrast limits from the J , H , and K images to assess how likely it is that the identified transit signal is an FP (see Section 4.4). To that end, we first subtracted the radial profiles of the central star’s point-spread function (PSF). We then convolved the images with circular apertures whose diameters are the same as the full width at half-maximum (FWHM) of the central star’s PSFs and computed standard

deviations as a function of projected separations from Gliese 12 in the convolved images. We calculated the central star’s flux in the apertures used at the image convolutions and divided the values of the standard deviations by the fluxes of the central star. As a result, we obtained the 5σ contrast limits shown in Figure 3. The J -, H -, and K -band contrast limits at $1''.0$ are 8.1, 8.5, and 9.0 mag, respectively. The source detected at $\approx 2''.4$ from Gliese 12 has a contrast equal to 9.23–9.27 mag depending on linearity corrections in the J -band master image (see Appendix A.1), yielding the source’s J -band magnitude as approximately 17.9 mag. The K -band contrast limit suggests that the faint source has a contrast greater than ≈ 9.8 mag, indicating that the source is fainter than ≈ 17.6 mag at K . We then referred to Gliese 12’s J - and K -band magnitudes in Table 1 to convert the contrast measurements of the source to the apparent magnitudes. We discuss in Section 4.4 that this faint object cannot be the source of the transit signal detected in the TESS data.

On UT 2023 August 15, we also obtained high-spatial-resolution images of the Gliese 12 system using NIRC2 and its K' ($\approx 2.12 \mu\text{m}$) filter on the Keck II Telescope (PI: C.

Table 1
Stellar Parameters of Gliese 12

Parameter	Value	Reference ^a
R.A. (J2000.0)	00 15 49.242	Gaia DR3
Decl. (J2000.0)	+13 33 22.32	Gaia DR3
$\mu_{R.A.} \cos \delta$ (mas yr ⁻¹)	+618.065 ± 0.039	Gaia DR3
$\mu_{\text{decl.}}$ (mas yr ⁻¹)	+329.446 ± 0.034	Gaia DR3
π (mas)	82.1938 ± 0.0326	Gaia DR3
Distance (pc)	12.1664 ± 0.0049	Gaia DR3
RUWE	1.198	Gaia DR3
Gaia <i>G</i> (mag)	11.399 ± 0.003	Gaia DR3
Gaia <i>B_p</i> (mag)	12.831 ± 0.003	Gaia DR3
<i>T</i> (mag)	10.177 ± 0.007	TIC
<i>J</i> (mag)	8.619 ± 0.020	2MASS
<i>K_s</i> (mag)	7.807 ± 0.020	2MASS
Spectral type	M3.0 V	Rei95
<i>T_{eff}</i> (K)	3296 ⁺⁴⁸ ₋₃₆	This work
log <i>g</i> (cgs)	5.21 ± 0.07	This work
<i>M_s</i> (<i>M_⊙</i>)	0.2414 ± 0.0060	This work
<i>R_s</i> (<i>R_⊙</i>)	0.2617 ^{+0.0058} _{-0.0070}	This work
ρ_s (ρ_{\odot})	13.5 ^{+1.2} _{-0.9}	This work
<i>L_{bol}</i> (10 ⁻³ <i>L_⊙</i>)	7.28 ± 0.15	This work
<i>L_X</i> (10 ²⁵ erg s ⁻¹)	6.0 ± 1.3	This work
log <i>R'_{HK}</i>	-5.23 ^{+0.10} _{-0.14}	This work
<i>P_{rot}</i> (days)	85	This work
<i>v sin i</i> (km s ⁻¹)	<2	This work
[Fe/H]	-0.32 ± 0.06	This work
[Na/H]	-0.37 ± 0.11	This work
[Mg/H]	-0.32 ± 0.22	This work
[Ca/H]	-0.37 ± 0.12	This work
[Ti/H]	-0.26 ± 0.26	This work
[Cr/H]	-0.34 ± 0.15	This work
[Mn/H]	-0.41 ± 0.19	This work
[Sr/H]	-0.22 ± 0.20	This work

Note.

^a Gaia DR3: Gaia Collaboration et al. (2023); TIC: Paegert et al. (2021); 2MASS: Skrutskie et al. (2006); Rei95: Reid et al. (1995).

Beichman). The images of Gliese 12 were corrected by the AO system for NIRC2, where we adopted PyWFS (Bond et al. 2020) as a wave-front sensor. PyWFS performs wave-front sensing at near-infrared wavelengths (mainly *H* band). Thus, PyWFS is an ideal choice to obtain high-quality PSF corrections for objects that are faint in the visual but bright in the infrared such as M-type stars (Uyama et al. 2023). The Keck/NIRC2 *K'*-band image after data processing is shown in Figure 3 with the 5 σ contrast curve at *K'*. In the image, we detect no object and did not recover the detection of the faint source identified in the Gemini/NIRI *J*-band image (see above). Appendix A.2 presents more details on our Keck/NIRC2 observations and imaging data reduction.

As done for the Gemini/NIRI images, we derived a contrast limit from the Keck/NIRC2 image for FP validation (see Section 4.4). We followed the same procedures adopted for the Gemini/NIRI observations except that the diameter of the circular aperture used for image convolution was set equal to λ/D (where *D* is the diameter of the Keck telescope).⁶⁴ Figure 3 shows the 5 σ contrast limit from the Keck/NIRC2 observations. The *K'*-band contrast limit is 9.0 mag at 1'' and

⁶⁴ This is because the FWHM of the unsaturated Br _{γ} PSF was measured to be smaller than λ/D .

slightly deeper (~ 0.2 mag on average) than the *K*-band contrast limit from Gemini/NIRI over 0''1–2''8.

3.2. Multiband Transit Photometry

We conducted photometric observations for four transits of Gliese 12 b that were expected to occur only if the true orbital period is 12.76 days (i.e., odd-numbered transits) using the multiband imagers MuSCAT2 (Narita et al. 2019) on the 1.52 m Telescopio Carlos Sánchez at the Teide Observatory in the Canary Islands, Spain, and MuSCAT3 (Narita et al. 2020) on the 2 m Faulkes Telescope North at the Haleakalā Observatory in Hawai'i, USA, on UT 2023 July 22 (MuSCAT3), 2023 August 16 (MuSCAT2), 2023 September 11 (MuSCAT3), and 2023 October 6 (MuSCAT2). Both MuSCAT2 and MuSCAT3 have four optical channels that enable simultaneous imaging in the *g*, *r*, *i*, and *z_s* bands. Each channel of MuSCAT2 is equipped with a 1k × 1k pixel CCD with a pixel scale of 0''44, providing a field of view (FoV) of 7'4. On the other hand, each channel of MuSCAT3 is equipped with a 2k × 2k pixel CCD with a pixel scale of 0''27, providing an FoV of 9'1. During the observations, we defocused the telescopes to avoid saturation such that the FWHM of the stellar PSF was 4''5–5''5, 7''0–8''0, 4''0–5''0, and 8''5–10''0 for the July 22, August 16, September 11, and October 6 observations, respectively. The exposure times were set at 7–60 s depending on the instrument, filter, and night.

After calibrating the obtained images for dark and flat field, we performed aperture photometry using the pipeline described in Fukui et al. (2011), with optimal aperture radii of 18–24 pixels (7''8–10''4) for the MuSCAT2 data and 15–19 pixels (4''1–5''1) for the MuSCAT3 data, depending on the band and night. We note that the photometric dispersions of the *g*-band data in all nights are much larger than the expected transit depth ($\sim 0.1\%$), and we therefore discard these data for the subsequent analyses of this Letter. The derived light curves in the *r*, *i*, and *z_s* bands from the four nights⁶⁵ are shown in Figure 4.

3.3. Doppler Spectroscopy

We observed Gliese 12 using the IRD instrument (Kotani et al. 2018) on the Subaru Telescope at Maunakea Observatory in Hawai'i, USA, between UT 2019 June 22 and UT 2022 November 25. Gliese 12 is in the master target list of the IRD-SSP campaign and has been intensively observed after initial screening observations (Harakawa et al. 2022). In IRD observations, wave-front-corrected object light is transferred to IRD's temperature-stabilized spectrograph in a vacuum chamber by a multimode fiber and dispersed by the spectrograph over the wavelength range of ≈ 930 –1740 nm with the resolving power (\mathcal{R}) of $\approx 70,000$ (Kotani et al. 2018). Using another multimode fiber, we obtained laser frequency comb spectra simultaneously with the target spectra, enabling us to calibrate RV drifts and instrument profile fluctuations (Hirano et al. 2020).

We took 76 spectra by spending exposure times of 280–1100 s for each data acquisition, with a signal-to-noise ratio (S/N) ranging from 20 to 158 around 1000 nm. We extracted 1D spectra from the raw 2D images taken with two H2RG (HAWAII-2RG) detectors of the IRD

⁶⁵ These time-series photometric data can be provided upon request to the first authors.

spectrograph based on the same procedures as used in the previous IRD papers (e.g., Kuzuhara et al. 2018; Hirano et al. 2020; Harakawa et al. 2022).

We applied the pipeline of Hirano et al. (2020) to the 1D spectra, providing the RV measurements of Gliese 12 reported in Appendix B. The pipeline divides a spectrum into many segments and calculates RVs from each segment, which are statistically combined into a single RV for each exposure. In this work, we adopted more constraining criteria than those adopted by Hirano et al. (2020) when clipping outlier RV measurements in the statistical combination of RVs, providing more stable RV measurements but slightly enlarging the internal errors. The zero-points of the IRD RV measurements were corrected using the postprocessing described by Gorrini et al. (2023). The internal error of RV measurements is typically 3.7 m s^{-1} .

We also observed Gliese 12 with CARMENES (Quirrenbach et al. 2014) in the framework of the CARMENES-TESS project for TESS follow-up of temperate planets (PI: E. Palle). CARMENES is a fiber-fed, dual-channel spectrograph at the 3.5 m Calar Alto telescope that operates simultaneously in the wavelength range between 0.52 and $1.71 \mu\text{m}$ in one shot. A dichroic at $0.96 \mu\text{m}$ splits the light that is injected into the two spectrograph channels, namely, VIS in the optical ($\mathcal{R} \approx 94,600$) and NIR in the near-infrared ($\mathcal{R} \approx 80,400$). We used the same standard operational mode as in the guaranteed time observations program for planet RV search (Ribas et al. 2023), in which target spectra were obtained simultaneously with the spectra from a Fabry–Pérot etalon for wavelength calibration using variable exposure times limited by $S/N=150$ and efficient scheduling (Garcia-Piquer et al. 2017). We channeled the CARMENES data through our pipelines, which include spectrum extraction and nightly zero-point corrections (Ribas et al. 2023, and references therein), telluric absorption corrections (Nagel et al. 2023), and RV determination with *serval* (Zechmeister et al. 2018). This work adopts the RVs measured with the CARMENES VIS channel, which are given in Appendix B. Because of the larger number of telluric-free lines in the optical spectrum of a mid-M dwarf with respect to the near-infrared (Reiners et al. 2018), the RVs from the CARMENES VIS channel have lower internal errors than IRD, of about 1.7 m s^{-1} .

3.4. X-Ray Flux Measurement

The European Space Agency X-ray telescope XMM-Newton observed Gliese 12 on UT 2018 June 16 (PI: J. H. M. M. Schmitt). XMM-Newton (Jansen et al. 2001) simultaneously operates two high-spectral resolution detectors (Reflection Grating Spectrometer) and an optical monitor, both of which did not attain a signal of Gliese 12, and three European Photon Imaging Camera (EPIC-pn and EPIC-MOS) detectors (sensitivity range 0.1–15 keV and 0.2–10 keV, respectively, and spectral resolution $E/\Delta E \sim 20\text{--}50$; Strüder et al. 2001; Turner et al. 2001). A 4.5σ detection of the star was achieved with an average 17.8 ks exposure on the three EPIC detectors. The X-ray spectra were analyzed using standard tools, revealing a typical one-temperature coronal spectrum at $\log T(\text{K}) = 6.44^{+0.12}_{-0.11}$ with an emission measure of $\log \text{EM}(\text{cm}^{-3}) = 48.39^{+0.14}_{-0.19}$. The fit assumed photospheric metallicity (see Section 4.1) and a small interstellar medium absorption of $N_{\text{H}} = 3 \times 10^{18} \text{ cm}^{-2}$. The spectral fit resulted in an X-ray (range 5–100 Å) luminosity of $L_{\text{X}} = 6.0 \pm 1.3 \times 10^{25} \text{ erg s}^{-1}$.

4. Analysis and Results

4.1. Stellar Parameters

Using a template spectrum created from the IRD spectra following Hirano et al. (2020), we carried out a line-by-line analysis to determine the effective temperature (T_{eff}), metallicity ($[\text{Fe}/\text{H}]$), and chemical abundances of Gliese 12. We followed the method developed by Ishikawa et al. (2020), which measures the equivalent widths (EWs) of the molecular lines and some atomic lines and compares them with those from theoretical synthetic spectra. We focused on the molecular lines of FeH and the atomic lines of Na, Mg, Ca, Ti, Cr, Mn, Fe, and Sr via the procedures adopted in the previous IRD-SSP papers (see Harakawa et al. 2022; Ishikawa et al. 2022; Hirano et al. 2023 for details). The T_{eff} and $[\text{Fe}/\text{H}]$ of Gliese 12 were derived to be $3344 \pm 44 \text{ K}$ and $-0.43 \pm 0.15 \text{ dex}$, respectively. Table 1 provides the abundances of the other atomic elements, which are available to characterize the Gliese 12 system in the future. We also analyzed the high-S/N CARMENES VIS and NIR template spectra of Gliese 12 using the spectral synthesis code *SteParSyn* (Tabernero et al. 2022), deriving Gliese 12’s T_{eff} , $\log g$, and $[\text{Fe}/\text{H}]$ to be $3363 \pm 70 \text{ K}$, $5.21 \pm 0.07 \text{ dex}$, and $-0.29 \pm 0.07 \text{ dex}$, respectively. The T_{eff} and $[\text{Fe}/\text{H}]$ values from the CARMENES spectra are consistent with those from the IRD spectra within their error bars. We computed the weighted average of the two $[\text{Fe}/\text{H}]$ measurements to be $-0.32 \pm 0.06 \text{ dex}$, which is given in Table 1. The relatively low metallicity agrees with the previous estimates from spectroscopic observations of Gliese 12, which range from -0.29 ± 0.09 to $-0.17 \pm 0.13 \text{ dex}$ (Newton et al. 2014; Maldonado et al. 2020). Houdebine et al. (2016) also inferred a lower metallicity of $-0.51 \pm 0.15 \text{ dex}$ from their metallicity–radius empirical correlation for M3V stars. We used the CARMENES spectra to constrain the projected rotational velocity of Gliese 12 to be $v \sin i < 2 \text{ km s}^{-1}$ (Reiners et al. 2018).

The metallicity of Gliese 12 is lower than the average value ($[\text{Fe}/\text{H}] = -0.05 \text{ dex}$) of the Galactic thin disk (Fuhrmann et al. 2017). However, the following kinematic analysis supports that this object belongs to the Galactic thin disk. We calculated the space velocities UVW of Gliese 12 relative to the local standard of rest (LSR) based on the astrometric measurements in Gaia DR3 (Gaia Collaboration et al. 2023) and the absolute RV (Soubiran et al. 2018). Then, we adopted the distance of 8.2 kpc between the Sun and the Galactic center (McMillan 2017), the height of the Sun above the Galactic midplane of 0.025 kpc (Jurić et al. 2008), and the solar motion relative to the LSR of $(U_{\odot}, V_{\odot}, W_{\odot}) = (11.10, 12.24, 7.25) \text{ km s}^{-1}$ (Schönrich et al. 2010). The calculated U , V , and W are -39.88 km s^{-1} , 38.92 km s^{-1} , and -23.47 km s^{-1} , respectively. These kinematics enabled us to compute the relative probability for the thick-disk-to-thin-disk membership (TD/D) using the method of Bensby et al. (2014). The computed TD/D is 0.16, which meets the criteria of $TD/D < 0.5$ to be classified as a likely thin disk star.

We also estimated the mass of Gliese 12 to be $M_s = 0.2414 \pm 0.0060 M_{\odot}$ using the K_s -band magnitude from the Two Micron All Sky Survey (2MASS; Skrutskie et al. 2006), the distance $d (=12.1664 \pm 0.0049 \text{ pc})$ derived from a parallax measurement for Gliese 12 in Gaia DR3, and an empirical mass– M_K relation for M dwarfs of Mann et al. (2019, their Equation (4) with $n=5$). To assign an error to the mass

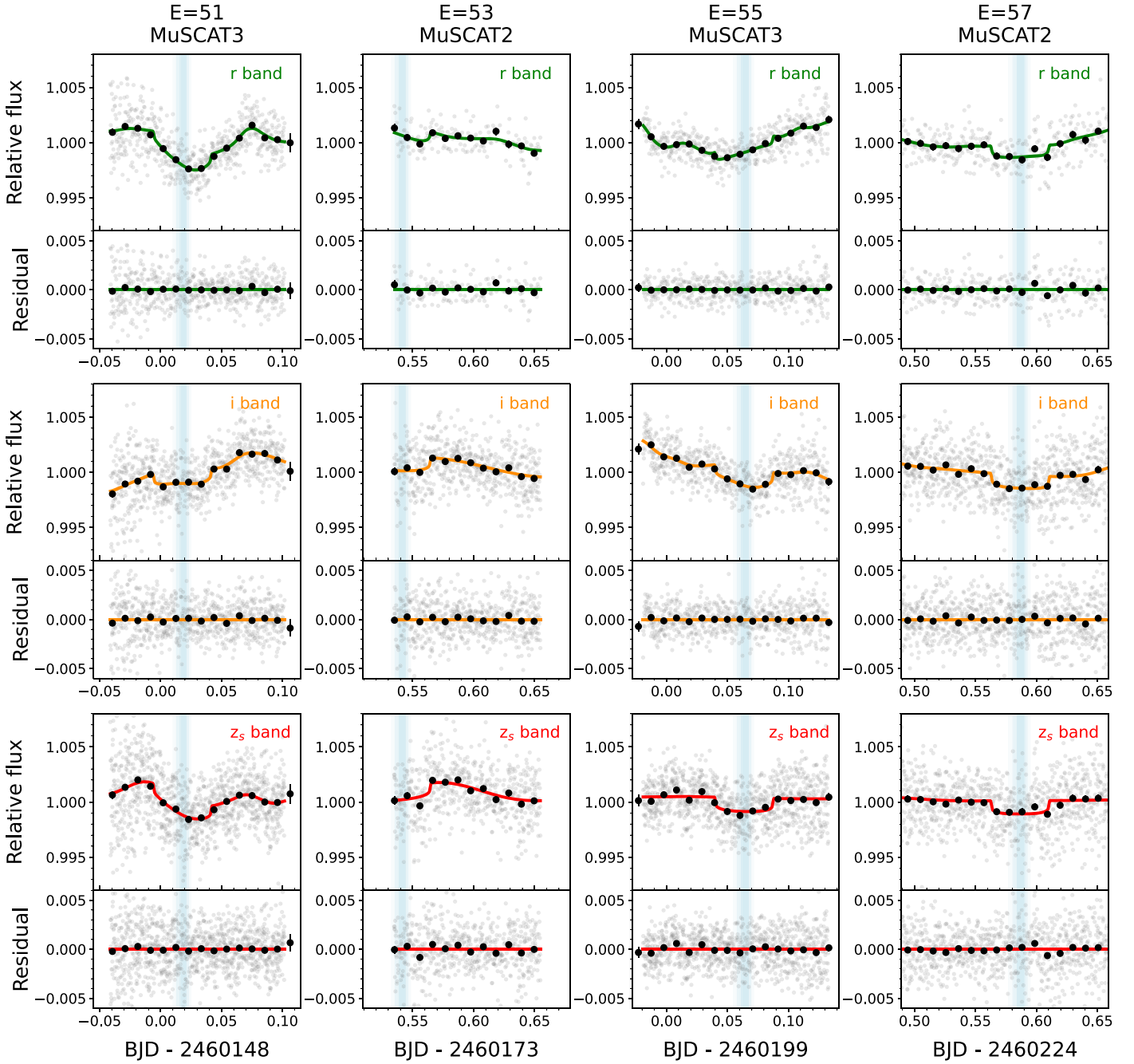


Figure 4. Individual transit light curves of Gliese 12 b obtained with MuSCAT2 and MuSCAT3. Columns from left to right show the data taken on the nights of UT 2023 July 22 (transit epoch = 51), August 16 (53), September 11 (55), and October 6 (57). The top, middle, and bottom rows are for the r , i , and z_s bands, respectively. The top and bottom panels in each panel pair show the undetrended light curve and its residuals from the best-fit transit+GP model (colored line), respectively (see details in Section 4.2.2). For both panels, gray dots and black circles indicate unbinned and 15 minute binned data, respectively. Darker to lighter blue vertical bands indicate the 1σ , 2σ , and 3σ credible regions, respectively, of the midtransit times predicted from P and $T_{c,0}$ derived from the analysis of the TESS light curves (Section 4.2.1).

estimation, we performed a Monte Carlo simulation adopted by Harakawa et al. (2022).

The T_{eff} , bolometric luminosity (L_{bol}), and radius (R_s) of Gliese 12 were determined by analyzing the spectral energy distribution (SED) created from the photometric measurements in the G , B_p , and R_p bands from Gaia DR3; the J , H , and K_s bands from 2MASS; and the $W1$, $W2$, $W3$, and $W4$ bands from AllWISE (Wright et al. 2010; Mainzer et al. 2011). The SED is modeled by synthetic spectra using the BT-Settl grid stellar atmospheric models of Allard (2014), following the procedure

described by Harakawa et al. (2022). We employed a Markov Chain Monte Carlo (MCMC) simulation using emcee (Foreman-Mackey et al. 2013) for the model parameters of T_{eff} , R_s , M_s , $[\text{Fe}/\text{H}]$, and d , imposing Gaussian priors on M_s , $[\text{Fe}/\text{H}]$, and d using the values listed in Table 1. Note that we expand the widths of the priors for M_s and $[\text{Fe}/\text{H}]$ by a factor of 5 to take into account the possible systematic uncertainties in the stellar atmospheric model grid. As a result, we obtained $R_s = 0.2617^{+0.0057}_{-0.0070} R_{\odot}$ and $T_{\text{eff}} = 3296^{+48}_{-36}$ K. From R_s , T_{eff} ,

and the Stefan–Boltzmann law, L_{bol} was calculated to be $7.28 \pm 0.15 \times 10^{-3} L_{\odot}$. We summarize the derived stellar parameter values in Table 1. Note that the derived T_{eff} from the SED analysis is consistent with the spectroscopically derived ones (3344 ± 44 K from IRD and 3363 ± 70 K from CARMENES) within $\approx 1\sigma$. We adopted the T_{eff} from the SED analysis for the rest of the Letter.

4.2. Confirmation of the Transit Signal

As described in Section 2, a transit signal with an orbital period of 12.76 days was initially detected in the TESS data from Sectors 42, 43, and 57 and was later reinforced by additional data from Sector 70. The multiple event detection statistic (MES) of the transit signal for all the available sectors, calculated by the SPOC pipeline, is 9.5, which is well above the detection threshold of $\text{MES} = 7.1$. However, although the transit depths individually measured for odd- and even-numbered transits are consistent with each other, the significance of the transit signal from the odd-numbered transits alone is only $\sim 1\sigma$ (see Figure 11 in Appendix C). Therefore, follow-up observations can confirm the 12.76 day transit signal by increasing the detection significance of odd-numbered transits. Confirming the transit signal by follow-up observations with spatial resolutions higher than TESS is also helpful to rule out the possibility that the transit signal detected by TESS comes from any contaminating stars within the TESS aperture. To this end, we separately analyze the TESS (Section 4.2.1) and ground-based (Section 4.2.2) data, the latter of which come only from odd-numbered transits, and compare the consistency in the transit model parameters between the two data sets.

4.2.1. Analysis of the TESS Light Curves

We first derived the transit model parameters from the TESS data alone by simultaneously modeling the TESS PDCSAP light curves of Sectors 43, 57, and 70 with a transit and systematics model. For the transit, we adopted the Mandel & Agol model implemented by PyTransit (Parviainen 2015) with the following parameters: log-scaled semimajor axis $\ln(a_R)$, where $a_R \equiv a/R_s$ and a is the semimajor axis; impact parameter b ; planet-to-star radius ratio k , where $k \equiv R_p/R_s$ and R_p is the planetary radius; orbital period P ; reference midtransit time $T_{c,0}$; and two coefficients u_1 and u_2 of a quadratic limb-darkening law. We assumed a circular orbit; i.e., the eccentricity e was fixed at 0.

Simultaneously with the transit model, we also estimated the time-correlated systematic noise in the light curves using a Gaussian process (GP) model implemented in celerite (Foreman-Mackey et al. 2017) with a kernel function of a stochastically driven, damped simple harmonic oscillator. For the GP, the modeled parameters were the frequency of undamped oscillation ω_0 , the scale factor to the amplitude of the kernel function S_0 , and the quality factor Q . We set Q to unity in all sectors and allowed ω_0 and S_0 (as $\ln \omega_0$ and $\ln S_0$, respectively) to be free for each sector.

We ran an MCMC analysis using emcee to estimate the posterior probability distributions of the parameters. For u_1 and u_2 , we applied Gaussian priors with the values and uncertainties given by LDTk (Parviainen & Aigrain 2015) for the stellar parameters of Gliese 12 in Table 1. Note that we enlarged the uncertainties of u_1 and u_2 provided by LDTk by a factor of

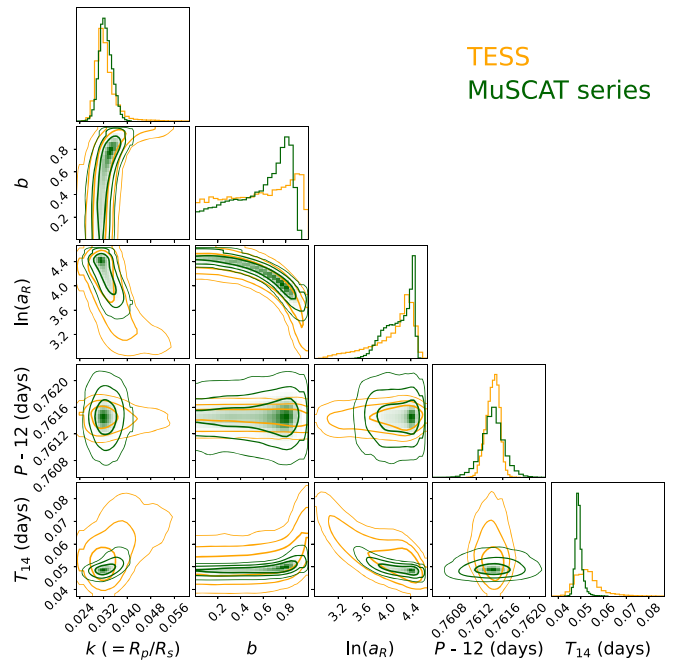


Figure 5. Corner plot for the posterior probability distributions of k , b , $\ln(a_R)$, P , and T_{14} from the analyses on the TESS (orange; Section 4.2.1) and MuSCAT series (green; Section 4.2.2) light curves, respectively. Thicker to thinner contours indicate the 1σ , 2σ , and 3σ credible regions. The posterior distributions of all parameters are in agreement with each other between the two data sets.

3, taking into consideration the possible systematics in the stellar models. We applied uniform priors for the other parameters. We started the analysis with initial values of our best guess, including $P = 12.76$ days. The priors and posteriors of the transit model parameters are summarized in Table 4 of Appendix D. Figure 5 shows the obtained posteriors of k , b , $\ln(a_R)$, P , and the transit duration T_{14} , which is calculated from the former four parameters. The model light curve for each sector predicted by the maximum-likelihood transit+GP model is shown in red in Figure 2.

4.2.2. Analysis of the Ground-based Light Curves

We analyzed the light curves obtained with MuSCAT2 and MuSCAT3 to confirm that (i) the transit signal detected by TESS indeed comes from Gliese 12 with the higher spatial resolution of the MuSCAT series, and (ii) the true orbital period is 12.76 days instead of twice it. Because all the light curves obtained with MuSCAT2 and MuSCAT3 correspond to odd-numbered transits of Gliese 12 b for the ephemeris of $P = 12.76$ days, while most of the transit signals in the TESS data come from even-numbered transits (four of the five full transits), the true orbital period can be confirmed by detecting or rejecting a transit signal in these MuSCAT2 and MuSCAT3 light curves.

Although a hint of transit signal is seen in each MuSCAT2 and MuSCAT3 light curve, the significance of each signal is marginal. We therefore simultaneously modeled all 12 MuSCAT2 and MuSCAT3 light curves with transit+GP models as follows.

For the transit, we applied the same model as for the analysis of the TESS light curves in Section 4.2.1. All model parameters are shared across all light curves except for u_1 and u_2 , which were let free for each band. For the GP model, we adopted an

approximate Matérn 3/2 kernel implemented in the `celerite` package with hyperparameters of $\ln \sigma$ and $\ln \rho$, where σ and ρ are the signal amplitude and length scale, respectively. We let $\ln \sigma$ be free for each light curve (each transit and each band) while letting $\ln \rho$ be shared within the three light curves of each transit assuming that the timescale of the time-correlated noise is common among all bands for a given night.

We then performed an MCMC analysis using `emcee` to calculate the posterior probability distributions of the model parameters. We applied uniform priors to all parameters except for u_1 and u_2 , to which Gaussian priors were applied in the same way as for the analysis in Section 4.2.1. We limited the values of $\ln \rho$ to -3 or larger so that the timescale of systematic trends is larger than the duration of the transit ingress and egress. We started the analysis setting the values of k , b , a_R , P , and $T_{c,0}$ to be the best-fit values obtained in the analysis of the TESS light curves. See Table 4 of Appendix D for the priors and posteriors of the transit model parameters.

We detected a constant-period transit signal with a radius ratio of $k = 0.0326_{-0.0019}^{+0.0025}$ at 17σ significance. In Figure 5, we show the derived posterior probability distributions of k , b , $\ln(a_R)$, P , and T_{14} in green. The distributions are highly consistent with those from the analysis of the TESS data, which are shown in orange. This consistency indicates that there does exist a transit signal in the MuSCAT2 and MuSCAT3 data that is consistent with the transit signal detected by TESS. We therefore conclude that (i) the transit signal detected in TESS comes from the photometric aperture of MuSCAT2 and MuSCAT3 ($\lesssim 10''$ in radius) centering on Gliese 12, and (ii) the true orbital period is 12.76 days.

4.3. RV Periodogram and Stellar Activity

We performed the generalized Lomb–Scargle (GLS) periodogram (Zechmeister & Kürster 2009) using a tool of `astropy` to search for a periodic signal in our RV measurements and activity indicators from IRD spectra, based on Harakawa et al. (2022). In the following periodogram analyses, false alarm probability (FAP) calculations are performed based on Baluev (2008). We did not analyze the RVs and indicators from CARMENES due to its limited observing span. The activity indicators that we used were FWHM, dV, CRX, and dLW. The method to compute the indicators with IRD data is described further in Harakawa et al. (2022). The FWHM and dV (or BiGauss) correspond to the FWHM and line asymmetry of the absorption lines, respectively. In addition, CRX and dLW correspond to the dependence of RV measurements on wavelength and differential line width, respectively. See Zechmeister et al. (2018) for the full definitions of the above activity indicators, except for dV, which is defined in Santerne et al. (2015). We show the results of the periodogram analyses in Figure 6. The periodogram analyzed for IRD RV measurements as well as for the activity indicators does not reveal any significant powers (FAP $< 5\%$) for periods shorter than 60 days, suggesting that (i) no RV signal from the transiting planet ($P = 12.76$ days) is detected (see Section 4.6 for completeness analysis), and (ii) the star is not chromospherically active. The chromatic activity of Gliese 12 was also investigated based on the measurement of the $H\alpha$ line by Newton et al. (2017), who found no emission feature in the line core, with its EW being $\text{EWH}\alpha = +0.064 \pm 0.024 \text{ \AA}$; a positive sign of the EW value indicates that $H\alpha$ is an absorption, suggesting that Gliese 12 is likely a Gyr old star

with low surface activity (e.g., Kiman et al. 2021). The insignificant $H\alpha$ emission is consistent with the weak X-ray activity (see Section 3.4) and the absence of flare-like events in the TESS light curves (Figure 2). Gliese 12’s X-ray luminosity ($L_X = 6.0 \pm 1.3 \times 10^{25} \text{ erg s}^{-1}$) is among the lowest detected in late-type stars (e.g., Caramazza et al. 2023) and indicates a quite low level of activity ($\log L_X/L_{\text{bol}} \approx -5.7$).

Finally, we searched for periodicity in archival light curves of Gliese 12 to measure its rotation period (P_{rot}). We extracted 6 yr of light curves observed in the g band between 2017 December and 2023 November from the ASAS-SN Sky Patrol⁶⁶ (Shappee et al. 2014; Kochanek et al. 2017). We detrended the ASAS-SN light curve using a quadratic function. We also analyzed the light curves from MEarth (2008 October to 2020 February; Berta et al. 2012) and SuperWASP (2008 August to 2010 December; Pollacco et al. 2006). The MEarth light curve was obtained with Telescope 7. The light curves were binned to nightly averages by first removing 3σ outliers and then computing weighted averages of photometric measurements. We performed GLS on them after 5σ clipping, producing the power spectra in Figure 6. We found a significant periodicity at ~ 85 days in the power spectrum of ASAS-SN. The power spectra of MEarth and SuperWASP show peaks at 83 days and 90 days, respectively, and these are close to ~ 85 days, though a higher peak appeared at ~ 108 days in the power spectrum of MEarth. Because the ASAS-SN light curve consists of the most continuous and frequently collected data points over many years among the three, we concluded that the periodicity at ~ 85 days is the most plausible value for P_{rot} . We also measured $\log R'_{\text{HK}}$ as in Perdelwitz et al. (2021) on six public spectra taken with HARPS (Mayor et al. 2003) between 2006 and 2010. The average value is in Table 1. Using the $\log R'_{\text{HK}}-P_{\text{rot}}$ relation of Astudillo-Defru et al. (2017), we estimated P_{rot} to be $P_{\text{rot,HandK}} = 60_{-16}^{+22}$ days, which is consistent with the value measured in the ASAS-SN light curve. The same periodicity can also be seen in the periodogram for the FWHM of IRD spectra at an FAP level of $\sim 5\%$. We attributed these signals to spot modulation associated with the stellar rotation. This long rotational period also supports that Gliese 12 is inactive and old.

4.4. Ruling Out FP Scenarios

A grazing eclipsing binary (EB), a hierarchical EB (HEB), and a background EB (BEB) aligned with Gliese 12 could mimic the transit signal detected in both TESS and MuSCAT series photometry. We ruled out those FP scenarios as follows. The Gemini/NIRI J -band images observed in 2009 detected a $J \approx 17.9$ mag source around Gliese 12, which was, however, undetected in the K -band images of NIRI (Section 3.1 and Appendix A.1). We first assessed whether or not that faint source can be an FP source. The blue $J - K$ color (< 0.3 mag) of this source indicates that it must not be a companion to Gliese 12 but a distant early-type (F- or earlier-type) star (Pecaut & Mamajek 2013). Given the Gaia DR3 astrometry (Gaia Collaboration et al. 2023), this source is estimated to be separated from Gliese 12 by $\approx 9''$ in Sector 43 of TESS, which is close enough to contaminate the TESS photometry. We constrained the source’s brightness in the TESS band with the conversion functions from the TESS input catalog (Stassun et al. 2018, their Equation jk and $joffset$) to be brighter than

⁶⁶ <https://asas-sn.osu.edu/>

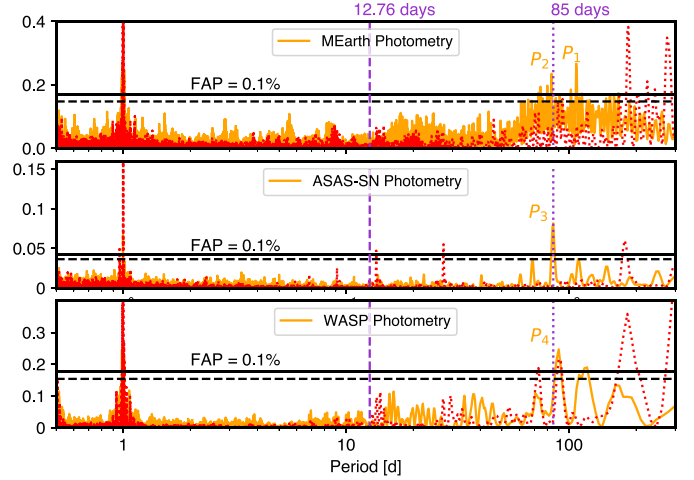
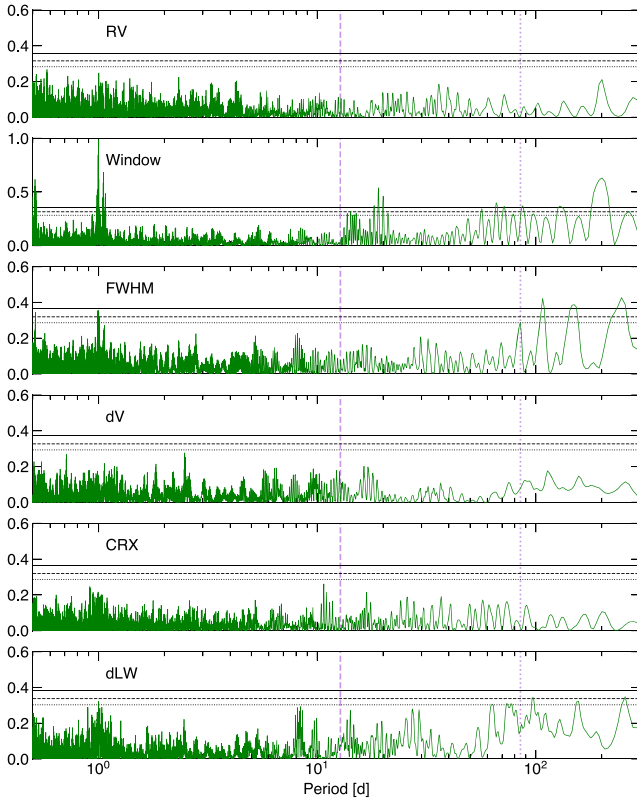


Figure 6. GLS periodogram analysis of the IRD RV measurements, the spectra, and the light curves of Gliese 12. The solid, dashed, and dotted horizontal lines in each panel correspond to FAPs of 0.1%, 1%, and 5%, respectively. The vertical dashed and dotted lines correspond to $P_{\text{orb}} \approx 12.76$ days and $P_{\text{rot}} \approx 85$ days, respectively. (Left) GLS powers (green lines) for RV, window function, FWHM, dV, CRX, and dLW are plotted in the panels from top to bottom. (Right) GLS powers for the MEarth (top), ASAS-SN (middle), and SuperWASP (bottom) light curves. Orange lines indicate GLS powers for the light curves, and red lines indicate their window functions. P_1 (=108 days), P_2 (=83 days), P_3 (=85 days), and P_4 (=90 days) in the panels indicate the periods of four peaks in the GLS powers.

$T = 18.4 \pm 0.8$ mag ($\Delta T < 8.1 \pm 0.8$ mag). Then, we converted the detected source’s J -band magnitude to its T magnitude under the limit of $J - K < 0.3$ mag. Thus, it could in principle be the cause of the transit signal (if a large fraction of its flux is occulted). However, this source is located outside of most of the photometric apertures for the MuSCAT2 and MuSCAT3 observations ($4''1$ – $7''8$ in radius for the first three transits), which finally confirmed the transit signal. This background source is therefore ruled out as the object causing the transit signal. Note that although the PDCSAP light curves do not correct for the dilution effect from this source due to the absence of this source in the Gaia DR3 catalog, the effect is so small that it can be neglected in the light-curve analyses (Sections 4.2.1 and 4.5).

Next, we considered other FP scenarios. Our RV data provide a mass constraint on the companion (see Section 4.6), ruling out the EB scenario. Furthermore, the constrained impact parameter ($b \lesssim 0.9$ at 3σ ; see Section 4.5 and Table 2) and boxy transit shape (see Figure 7) eliminate the possibility of grazing transit geometries. We simulated eclipses for a range of plausible HEBs following the method of Mori et al. (2022), which was based on Bouma et al. (2020). Our simulations provided no configuration that can match the transit depth and transit shape observed in multiple bands with TESS and MuSCAT series. The low value of the renormalized unit weight error (RUWE) from \Gaia DR3 (1.198; see Table 1) also supports that Gliese 12 is a single star (Belokurov et al. 2020).

The probability of a chance alignment of a BEB is low given the target’s location far from the Galactic plane ($b \approx -48^\circ$).

Our AO imaging at K' rules out blends down to $0''.2$ for objects with $\Delta K' < 5$ mag (see Section 3.1), and archival images reveal no bright background stars near the current position of Gliese 12 (see Figure 1).

Finally, we computed the FP probability (FPP) of the case $P_{\text{orb}} = 12.76$ days for Gliese 12 with the Python software program TRICERATOPS (Giacalone & Dressing 2020). We then used the TESS light curve phase-folded at the given period, the Keck/NIRC2 AO contrast curve at K' given in Figure 3, and the reported stellar parameters in Table 1. We ran TRICERATOPS 20 times and computed an upper limit on the FPP of 0.7% (3σ). This value is below the threshold of $\text{FPP} < 1.5\%$ prescribed by Giacalone et al. (2021), further supporting that Gliese 12 b is a bona fide planet based on statistical validation.

4.5. Joint Analysis of RVs and Transit Light Curves

Although we did not detect any significant planetary signals in the RV data (Section 4.3), these data are still useful for placing upper limits on the planetary mass and orbital eccentricity. To best measure or constrain the orbit, mass, and radius of Gliese 12 b, we modeled all the transit (TESS, MuSCAT2, and MuSCAT3) and RV (IRD and CARMENES) data simultaneously. The model parameters for the RV data are as follows: RV semiamplitude K ; orbital period P ; two eccentricity parameters, $e \sin \omega$ and $e \cos \omega$, where e and ω are the eccentricity and argument of periapsis, respectively; reference time of inferior (midtransit) passage $T_{\text{c,rv}}$; RV zero-point for each instrument $v_{0, \text{IRD}}$ and $v_{0, \text{CAR}}$; and RV jitter for

Table 2
MCMC Fitting Results for RV and Transit Light-curve Data

Parameter	Median and $\pm 1\sigma$ Interval Fitted Parameters	3σ Range ^a	Prior ^b
b	$0.759^{+0.049}_{-0.114}$	(0.069, 0.904)	$\mathcal{U}(0, 1)$
$k (=R_p/R_s)$	0.0336 ± 0.0015	(0.0292, 0.0381)	$\mathcal{U}(0, 0.4)$
$\sqrt{e} \sin \omega$	0.09 ± 0.29	(-0.61, 0.66)	$\mathcal{U}(-1, 1)$
$\sqrt{e} \cos \omega$	0.00 ± 0.26	(-0.63, 0.65)	$\mathcal{U}(-1, 1)$
$\ln \rho_s (\rho_\odot)$	2.62 ± 0.08	(2.38, 2.84)	$\rho_s = \mathcal{N}(13.5, 1.2)$ ($\rho_s > 13.5$) $\rho_s = \mathcal{N}(13.5, 0.9)$ ($\rho_s \leq 13.5$)
K (m s^{-1})	$1.13^{+0.56}_{-0.54}$	< 2.78	$\mathcal{U}(0, 10^2)$
$\sigma_{\text{jit, IRD}}$ (m s^{-1})	$2.80^{+0.66}_{-0.69}$	(0.20, 4.83)	$\mathcal{U}(0, 10^2)$
$\sigma_{\text{jit, CAR}}$ (m s^{-1})	$2.20^{+0.76}_{-0.61}$	(0.50, 5.37)	$\mathcal{U}(0, 10^2)$
Derived Parameters			
Orbital period, P (days)	12.761408 ± 0.000050	...	
Reference transit time, $T_{c,0}$ (BJD)	2459497.1865 ± 0.0026	...	
Transit duration, T_{14} (hr)	1.20 ± 0.09	(0.96, 1.74)	
Planet radius, R_p (R_\oplus)	$0.958^{+0.046}_{-0.048}$	(0.815, 1.104)	
Planet mass, M_p (M_\oplus)	$1.57^{+0.78}_{-0.75}$	< 3.87	
Eccentricity, e	$0.11^{+0.14}_{-0.08}$	< 0.50	
Orbital Inclination, i_{orb} (deg)	$89.194^{+0.059}_{-0.052}$	(89.013, 89.873)	
Semimajor axis, a (au)	0.0668 ± 0.0024	(0.0596, 0.0739)	
Scaled semimajor axis, a/R_s	54.9 ± 1.4	(50.8, 59.3)	
Equilibrium temp., T_{eq} (K) (albedo = 0) ^c	$314.6^{+6.0}_{-5.4}$	(299.5, 333.5)	
Equilibrium temp., T_{eq} (K) (albedo = 0.3) ^c	$287.8^{+5.5}_{-5.0}$	(274.0, 305.1)	
Insolation, S (S_\oplus)	$1.62^{+0.13}_{-0.11}$	(1.33, 2.05)	

Notes.

^a The two-sided 99.73% confidence intervals are shown for all parameters except for the positive-valued parameters that are consistent with 0 within 3σ (K , e , and M_p), for which the one-sided 99.73% confidence intervals are shown.

^b $\mathcal{U}(a, b)$ denotes a uniform distribution between a and b , and $\mathcal{N}(a, b)$ denotes a normal distribution with the mean of a and variance of b^2 .

^c A uniform surface temperature is assumed.

each instrument $\sigma_{\text{jit, IRD}}$ and $\sigma_{\text{jit, CAR}}$, where CAR stands for CARMENES.

The parameters for the transit model are the same as for Sections 4.2.1 and 4.2.2, but this time the assumption of a circular orbit was removed. We also let individual midtransit times $T_{c,i}$ for both the TESS and MuSCAT series data sets be free to take into account possible transit timing variations (TTVs). In addition, we used log stellar density $\ln \rho_s$ as a fitting parameter instead of a_R , which was converted from ρ_s and P using the equation $a_R = (\rho_s GP^2/3\pi)^{1/3}$ (assuming $k^3 \ll 1$), where G is the gravitational constant. We assumed that the radius ratio k is common across all bands.

With the above parameterization, we performed an MCMC analysis using `emcee`. In the analysis, we fixed $T_{c,rv}$ and P at the best-fit values of $T_{c,0}$ and P , respectively, derived from the analysis of the TESS data (Section 4.2.1). For the prior on $\ln \rho_s$, we applied a two-sided Gaussian in the form of ρ_s , adopting the value estimated in Section 4.1 ($\rho_s = 13.5^{+1.2}_{-0.9} \rho_\odot$). For the priors on the eccentricity parameters, we applied the joint probability distribution for e and ω of Kipping (2014; Equation (23) of that paper), who adopted the beta function as the underlying prior for e . For the two coefficients of the beta function, we adopted $\alpha = 1.18$ and $\beta = 6.34$ from Sagar & Ballard (2023), which were derived for singly transiting planets around early-to-mid-M dwarfs. The hyperparameters of the GP models for both the TESS and MuSCAT series' light curves were fixed to the best-fit values derived from the analyses in Sections 4.2.1 and 4.2.2, respectively. For all the other parameters, uniform priors were applied. With a total of 28 free parameters, we ran 56

walkers $\times 10^5$ MCMC steps after convergence for calculating posterior probability distributions. We assessed convergence by verifying that two independent MCMC runs yielded consistent posterior probability distributions for all parameters.

The median values and 1σ boundaries of the fitting parameters and derived planetary parameters are reported in Table 2. We found that Gliese 12 b is an Earth-sized planet with a radius of $0.958^{+0.046}_{-0.048} R_\oplus$. We show detrended, phase-folded, and binned light curves from TESS, MuSCAT2, and MuSCAT3 created using the best-fit parameter values, as well as phase-folded RV data along with the posterior RV models, in Figure 7. In Appendix E, we provide a corner plot for the derived posterior probability distributions of a subset of the model parameters.

Applying a linear regression to the measured individual midtransit times $T_{c,i}$, we refined $T_{c,0}$ and P to be 2459497.1865 ± 0.0026 in BJD and 12.761408 ± 0.000050 days, respectively. In Appendix E, we also show a plot of the midtransit times with the refined ephemeris subtracted. We found no significant TTVs in the data with a χ^2 value of 8.6 with 8 degrees of freedom for the linear ephemeris fit.

4.6. Completeness of IRD Data for Planet Detection

We produced a detection completeness map of IRD RV measurements to constrain the presence of additional planets in the Gliese 12 system. To this end, we ran Monte Carlo simulations over the $\log P_{\text{orb}}$ versus $\log(m \sin i)$ grids, where P_{orb} and $m \sin i$ indicate the orbital period (in days) and the minimum mass (in units of M_\oplus) of a planet, respectively. We

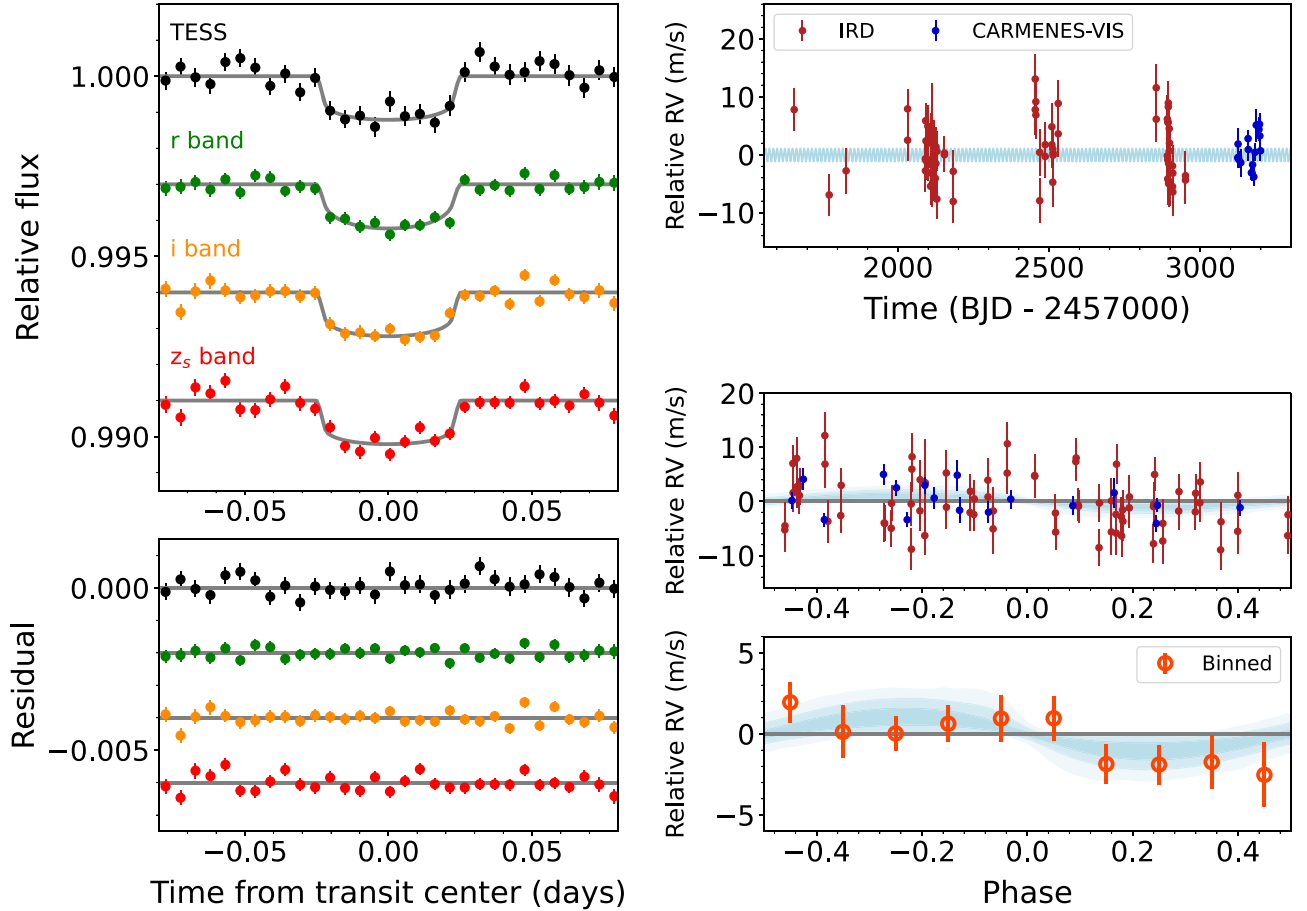


Figure 7. (Top left) Detrended (with the best-fit GP models), phase-folded, and 450 s binned transit light curves of Gliese 12 b. The data taken in the TESS, r , i , and z_s bands are plotted from top to bottom. The gray lines represent the best-fit transit models. Each light curve is vertically shifted by an arbitrary value for display purposes. (Bottom left) Same as the top left panel, but residuals from the best-fit transit models are shown. (Top right) RV time series of Gliese 12 measured with IRD (red) and CARMENES (blue) along with the best-fit Keplerian model (light blue). The error bars represent 1σ uncertainties without including RV jitters. (Middle right) Same as the top right panel, but the data are phase-folded with the orbital period of Gliese 12 b. The error bars here represent 1σ uncertainties taking RV jitters into account. The darkest, second-darkest, and lightest light blue colors indicate the 1σ , 2σ , and 3σ confidence regions calculated from the joint analysis, respectively. (Bottom right) Same as the middle right panel, but the data are binned into 10 equally spaced bins.

varied $\log P_{\text{orb}}$ from 0 to 3 with 0.05 increments and $\log(m \sin i)$ from 0 to 2 with 0.05 increments. We randomly sampled the orbital parameters of a planet (eccentricity, argument of periastron, and time of periastron) at each grid point, with Gliese 12’s mass fixed to the value in Table 1; the value of eccentricity was obtained from a Rayleigh distribution with $\sigma = 0.19$ (Sagear & Ballard 2023), which is appropriate for a single planet around an early-to-mid-M dwarf. We then simulated a time series of Keplerians at each grid point, to which measurement uncertainties were added by sampling from zero-mean normal distributions with standard deviations equal to the internal errors of the IRD data set, as well as an additional RV jitter based on our estimate in Section 4.5. The periodogram analyses described in Section 4.3 were applied to the artificial RVs, assuming that a signal with power corresponding to $\text{FAP} \leq 1\%$ is a detection. We repeated this procedure 100 times, thereby generating a map of detection statistics at each grid point with which to draw conclusions about the presence of planets around Gliese 12, which is shown in Figure 8.

Between 1 and 10 days, our simulations rule out the presence of a Neptune-mass planet ($10\text{--}20 M_{\oplus}$) and show that there are most likely no massive super-Earths ($\approx 7\text{--}10 M_{\oplus}$). Meanwhile, the existence of a low-mass super-Earth is not ruled out, as only

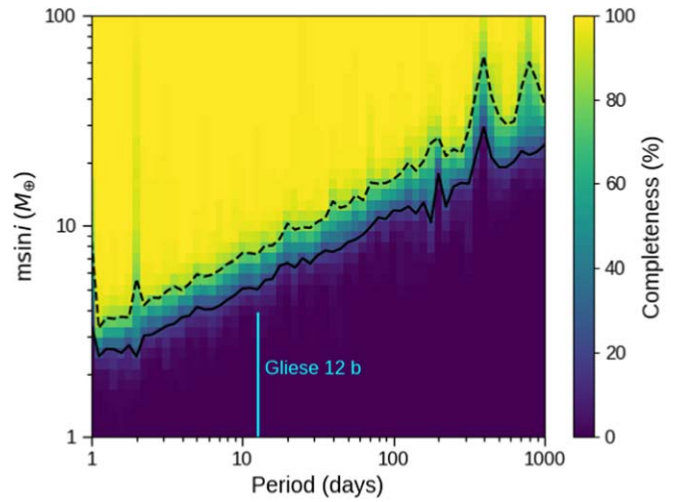


Figure 8. Detection completeness of a simulated planet around Gliese 12. The horizontal axis and vertical axis indicate the orbital period and the minimum mass ($m \sin i$) of a planet, respectively. The color bar shows the percentage of instances of a simulated planet that is detected. The solid and dashed lines correspond to the detection completeness of 20% and 80% of simulated planets, respectively. The vertical cyan line represents the orbital period (≈ 12.76 days) and mass range ($\leq 3\sigma$) of Gliese 12 b (see Section 4.5).

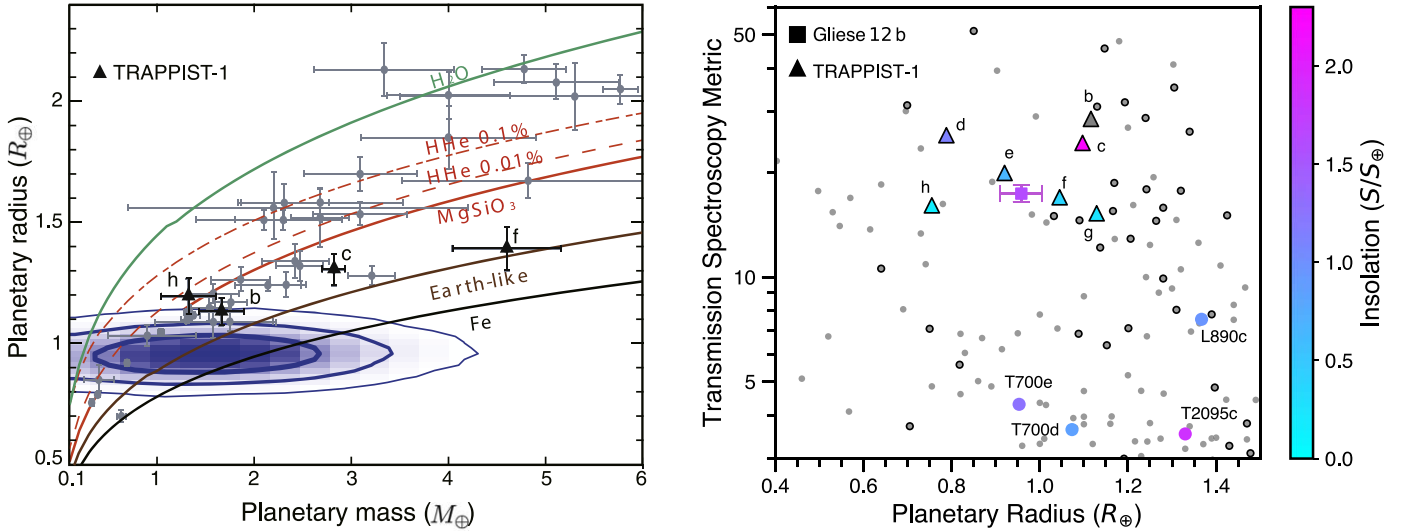


Figure 9. (Left) Mass–radius relation for planets with masses below $6 M_{\oplus}$ around M dwarfs with $T_{\text{eff}} \leq 3900$ K. Gray circles are all the known exoplanets in this mass range taken from the NASA Exoplanet Archive (2023a). We plot the 1σ , 2σ , and 3σ contours of the mass and the radius of Gliese 12 b. The colored curves show interior models of planets that are composed of pure water, pure silicate, Earth-like rock, and pure iron. We adopted $T_{\text{eq}} = 312.9$ K and the AQUA (Haldemann et al. 2020), Birch–Murnaghan, and Vinet EoS (Seager et al. 2007; Zeng & Sasselov 2013) as equations of state of H_2O , MgSiO_3 , and $\epsilon - \text{Fe}$. The dashed and dashed-dotted curves show the mass–radius relation of a rocky core with a hydrogen-rich atmosphere of 0.01 wt% and 0.1 wt%, respectively. (Right) TSM values calculated for Gliese 12 b (square) and other small ($R \leq 1.5 R_{\oplus}$) exoplanets against their planetary radii. Colored symbols indicate the planets whose insolation flux (S) is $< 2.3 S_{\oplus}$, with colors scaled by S (as shown by the color bar). The symbols with black edges represent the planets with masses constrained by methods other than an empirical mass–radius relation. The planets within this range are labeled: T700, L890, and T2095 stand for TOI-700 (Gilbert et al. 2023), LP 890-9 (Delrez et al. 2022), and TOI-2095 (Murgas et al. 2023), respectively. The planets with $S > 2.3 S_{\oplus}$ are indicated by gray symbols. On both the left and right panels, the planets around TRAPPIST-1 are plotted with triangles.

20% of the total simulations were able to detect a planet as massive as $\sim 4 M_{\oplus}$ at $P_{\text{orb}} = 5$ days. For $10 \text{ days} < P_{\text{orb}} < 30$ days, the detection completeness is higher than 80% only for planets heavier than massive super-Earths, while for planets with mass $\gtrsim 50 M_{\oplus}$, it is above 80% for almost the entire range of P_{orb} . In summary, our completeness simulations reveal that there are probably no massive super-Earths at $P_{\text{orb}} = 1\text{--}30$ days, no Neptune-mass planets at $P_{\text{orb}} < 150$ days, and no giant planets more massive than Saturn ($\approx 100 M_{\oplus}$) at $P_{\text{orb}} < 1000$ days.

5. Discussion and Summary

We have identified an Earth-sized planetary candidate transiting the nearby mid-M dwarf Gliese 12 from the TESS observations and subsequently validated its planetary nature from the ground-based follow-up observations including multiband transit photometry with MuSCAT2 and MuSCAT3, high-contrast imaging with NIRC2, and RV measurements with IRD and CARMENES. We have revealed that the planet, Gliese 12 b, has a radius of $0.96 \pm 0.05 R_{\oplus}$, a 3σ mass upper limit of $3.9 M_{\oplus}$, and an orbital period of 12.76 days. We have found no additional planet with a mass larger than Neptune (Saturn) within an orbital period of 50 days (1000 days) based on a 4 yr long RV monitoring with IRD.

Figure 9 shows the mass–radius relation for planets less massive than $6 M_{\oplus}$ around M dwarfs. The weak constraint on the mass of Gliese 12 b from our RV measurements allows various internal compositions for this planet. Within the measured upper limit on the mass, Gliese 12 b could be a dense Earth-sized planet (even as dense as pure iron). This possibility is intriguing because such a high-density planet has only rarely been discovered around relatively metal-poor stars (e.g., Barros et al. 2022) such as Gliese 12 ($[\text{Fe}/\text{H}] = -0.32 \pm 0.06$). Alternatively, Gliese 12 b could be volatile-

rich. If the mass of Gliese 12 b is well below $1 M_{\oplus}$, then Gliese 12 b could be either a rocky planet with a small mass fraction of a hydrogen-rich atmosphere or a water-rich planet without a hydrogen-rich atmosphere (see Figure 9), the latter of which would indicate either orbital migration or an efficient inward transport of icy material from outside the snow line. Thus, precisely determining the mass of Gliese 12 b via follow-up RV observations is important in the context of the formation and evolution of Earth-sized planets and will undoubtedly be the subject of future works.

With an orbital period of 12.76 days, Gliese 12 b is likely to be tidally locked. The insolation flux that Gliese 12 b receives from the host star is calculated to be $1.62^{+0.13}_{-0.11} S_{\oplus}$, where S_{\oplus} is the insolation of the Earth. This makes its location even closer to the star than the inner edge of the HZ for a tidally locked planet orbiting a star with an effective temperature of 3300 K ($\approx 1.3 S_{\oplus}$; Kopparapu et al. 2017). Thus, Gliese 12 b is less likely to retain a stable ocean, although the inner edge of the HZ could depend on several other factors as well, such as the total atmospheric pressure, the planetary mass, and the land-to-ocean fraction (e.g., Kodama et al. 2019). Gliese 12 b is more likely to be in the runaway greenhouse state, where the planetary atmosphere contains water vapor, or in a dry state after water loss by escape, where the atmosphere contains little water vapor. Gliese 12 b is therefore an intriguing target for future atmospheric studies to understand the atmospheric state of potentially rocky planets near the inner edge of the HZ.

The proximity ($d = 12$ pc) and brightness ($J = 8.6$ mag) of the system make Gliese 12 b a still-uncommon, low-insolation, and potentially terrestrial planet that is amenable to atmospheric characterization through transmission spectroscopy. Using the empirical mass–radius relationships of Chen & Kipping (2017) and Louie et al. (2018), we convert Gliese 12 b’s radius to a mass of $0.83^{+0.15}_{-0.14} M_{\oplus}$. With this mass

determination, we followed Kempton et al. (2018) to determine the transmission spectroscopy metric (TSM) value of Gliese 12 b to be $17.4_{-0.9}^{+1.0}$, which is compared with known planets with radii smaller than $1.5 R_{\oplus}$ in the right panel of Figure 9. We note that the theoretical mass–radius relation shown in Figure 9 limits the TSM value of Gliese 12 b to higher than ~ 7 . The higher the TSM value of a planet, the more suitable it is for atmosphere transmission spectroscopy (see Kempton et al. 2018). All the data for the known (confirmed) planets are taken from NASA Exoplanet Archive (2023b).⁶⁷ In the figure, we highlight the planets that receive insolation fluxes (S) lower than $2.3 S_{\oplus}$ (which is approximately equivalent to the insolation flux onto TRAPPIST-1 c). Within the parameter range shown here, only the TRAPPIST-1 planets and Gliese 12 b have TSM values higher than 10, placing Gliese 12 b in the still-limited sample of temperate and potentially terrestrial planets that are suitable for transmission spectroscopy.

The actual detectability of atmospheric signatures, however, depends on the amount and composition of the atmosphere, which can be affected by the XUV irradiation from the host star. A recent JWST/MIRI observation revealed that TRAPPIST-1 c has no thick atmosphere like that of Venus, which may be due to atmospheric escape caused by strong XUV radiation and stellar winds from the host star (Lincowski et al. 2023; Zieba et al. 2023; Teixeira et al. 2024). The semimajor axis of TRAPPIST-1 c is 0.016 au (Agol et al. 2021) from the host, which has an XUV luminosity of $L_{\text{XUV}} \approx 0.7\text{--}1.8 \times 10^{27} \text{ erg s}^{-1}$ (Wheatley et al. 2017; Becker et al. 2020). On the other hand, we used our coronal model as in Sanz-Forcada et al. (2011, and references therein) to estimate the XUV luminosity of Gliese 12 to be $L_{\text{XUV}} \approx 4.4 \times 10^{26} \text{ erg s}^{-1}$ (for the range of 5–920 Å), which is even lower than that of TRAPPIST-1. Since the semimajor axis of Gliese 12 b (0.067 au) is nearly 4 times larger than that of TRAPPIST-1 c, Gliese 12 b is approximately 30–70 times less irradiated in XUV than TRAPPIST-1 c. Even with this currently weak XUV irradiation, Gliese 12 b may have lost a large part of its primordial (hydrogen-rich) atmosphere considering that the XUV luminosity of the star must have been higher in the past (e.g., Penz & Micela 2008; Johnstone et al. 2021). Nevertheless, there is a higher probability that Gliese 12 b has a more significant secondary (C-, N-, and/or O-rich) atmosphere than TRAPPIST-1 c, because the amount of secondary atmosphere is considered to be regulated by the supply of gases (e.g., outgassing) and the escape driven by the current XUV irradiation and stellar wind.

Atmospheric characterization of Gliese 12 b using transmission spectroscopy with JWST would therefore allow direct comparison to other Earth-sized exoplanets like the TRAPPIST-1 worlds. To explore the feasibility of observing the atmosphere of Gliese 12 b with JWST, we simulate its transmission spectrum using the radiative transfer and retrieval code TauREx3 (Al-Refaie et al. 2021), assuming that the density of Gliese 12 b is comparable to that of the Earth. Since the actual atmospheric composition of this planet is difficult to know a priori, we explore five simple cases to highlight the telescope performances.

1. Case 1: a reference scenario with remaining primordial gas (H_2 and He). The atmosphere is simulated at chemical equilibrium using the GGChem code (Woitke & Helling 2021) with a metallicity of $100\times$ solar.
2. Case 2: a Titan-like atmosphere composed of 95% N_2 and 5% CH_4 with constant altitude abundance profiles. A fully opaque cloud layer at 0.1 bar is also added.
3. Case 3: a water-world scenario with a 100% H_2O atmosphere and a fully opaque cloud layer similar to case 2.
4. Case 4: a Venus-like case with a 100% CO_2 atmosphere and a fully opaque cloud layer similar to case 2.
5. Case 5: a clear Venus-like case. Same as case 4 but without clouds.

In these models, the atmosphere is simulated using the TauREx transit forward model and assuming a plane-parallel atmosphere with 100 layers evenly spaced in log-space between 10 and 10^{-5} bars. We assumed an isothermal temperature–pressure profile at the equilibrium temperature of the planet. We modeled the atmosphere at the native resolution $\mathcal{R} = 15,000$ of the cross section (H_2O : Polyansky et al. 2018; CH_4 : Yurchenko et al. 2017; Chubb et al. 2020; CO_2 : Chubb et al. 2020; Yurchenko et al. 2020) and then convolved the resulting spectrum with the JWST instrument response function for NIRSpec (Jakobsen et al. 2022) grisms G140H, G235H, and G395H, which we obtained via the online Pandexo tool (Batalha et al. 2017). We note that to avoid $>80\%$ saturation, G140H and G235H require three and five groups, respectively, which would make the characterization of the nondestructive ramps more difficult than with G395H, for which seven groups is optimal. We display the final models and observed spectra for six stacked observations with each JWST instrument configuration in Figure 10. Note that the simulated observations have been binned down to $\mathcal{R} = 50$ for visualization purposes. The simulated JWST transmission spectra of Gliese 12 b demonstrate detectable atmospheric features for a range of compositions, underscoring the potential to characterize this terrestrial exoplanet using a modest amount of JWST time. Furthermore, transit photometry with JWST for an active star like TRAPPIST-1 is disturbed by the contamination of flares (Howard et al. 2023), which should be less problematic for Gliese 12 due to its quiescent nature.

Given that Gliese 12 is only the second M dwarf system within 30 pc hosting Earth-sized planets with insolation less than $2 S_{\oplus}$, following TRAPPIST-1, it will undoubtedly be the subject of many future studies as a benchmark system. These studies will help reveal the diversity of atmospheres and climates on temperate rocky planets, furthering our understanding of planetary environments beyond our solar system.

Acknowledgments

We thank the reviewer, whose careful reading of the manuscript and excellent suggestions have improved the quality of this Letter. We thank Andrew W. Stephens and Sandy Leggett for data reduction support for the Gemini/NIRI data. We acknowledge that the TRES team posted the results of their spectroscopic observations of Gliese 12 spanning 5 yr to ExoFOP-TESS soon after TOI-6251.01 was released, showing no large RV variations ($\text{rms} = 21 \text{ m s}^{-1}$).

Funding for the TESS mission is provided by NASA’s Science Mission Directorate. We acknowledge the use of

⁶⁷ For those planets lacking a proper mass constraint in the catalog (93 out of 133), we estimated the mass using the radius and a mass–radius relation in the same way as was done for Gliese 12 b.

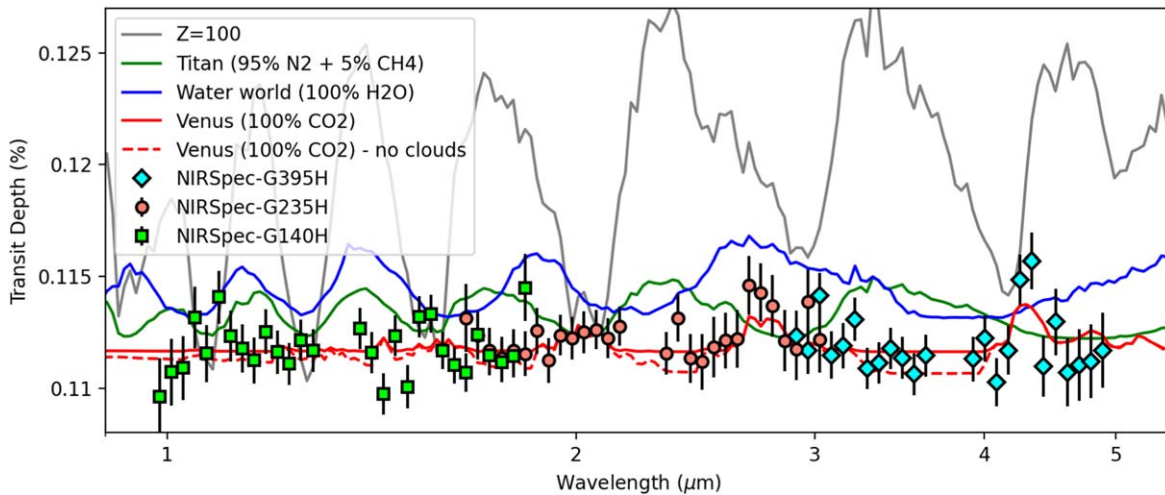


Figure 10. Predicted transmission spectra for Gliese 12 b, assuming an isothermal temperature–pressure profile, an Earth-like density, and several different cloud-free compositions: primordial H_2 and He at $100\times$ solar metallicity, Titan-like, water world, and Venus-like. For the Venus-like scenario, we also show a model including 0.1 bar fully opaque clouds. We show simulated data assuming the cloudy Venus scenario and six transits per JWST/NIRSpec grism: G140H (green squares), G235H (red circles), and G395H (blue diamonds).

public TESS data from pipelines at the TESS Science Office and at the TESS Science Processing Operations Center (SPOC). Resources supporting this work were provided by the NASA High-End Computing (HEC) Program through the NASA Advanced Supercomputing (NAS) Division at Ames Research Center for the production of the SPOC data products. This Letter includes data collected by the TESS mission that are publicly available from the Mikulski Archive for Space Telescopes (MAST). All the TESS data used in this Letter can be found in MAST: doi:[10.17909/psfb-yg51](https://doi.org/10.17909/psfb-yg51).

The Gemini data that we used in this work are publicly available from the Gemini Observatory Archive (GOA; <https://archive.gemini.edu>) under the program GN-2009B-Q-10 (PI: Sergio Dieterich), whose abstract is shown at <https://archive.gemini.edu/programinfo/GN-2009B-Q-10>.

This work is based on observations obtained with XMM-Newton, an ESA science mission with instruments and contributions directly funded by ESA Member States and NASA. This work has made use of data from the European Space Agency (ESA) mission Gaia (Gaia Collaboration et al. 2016; <https://www.cosmos.esa.int/gaia>), processed by the Gaia Data Processing and Analysis Consortium (DPAC; <https://www.cosmos.esa.int/web/gaia/dpac/consortium>).

Funding for the DPAC has been provided by national institutions, in particular the institutions participating in the Gaia Multilateral Agreement. This work used the data from the Second Palomar Observatory Sky Survey (POSS-II), which was made by the California Institute of Technology with funds from the National Science Foundation, the National Geographic Society, the Sloan Foundation, the Samuel Oschin Foundation, and the Eastman Kodak Corporation. This Letter makes use of data from the MEarth Project, which is a collaboration between Harvard University and the Smithsonian Astrophysical Observatory. The MEarth Project acknowledges funding from the David and Lucile Packard Fellowship for Science and Engineering; the National Science Foundation under grants AST-0807690, AST-1109468, AST-1616624 and AST-1004488 (Alan T. Waterman Award); the National Aeronautics and Space Administration under grant No. 80NSSC18K0476 issued through the XRP Program; and the John Templeton Foundation. This work is based on HARPS

data obtained from the ESO Science Archive Facility: the HARPS data are based on observations made with ESO Telescopes at the La Silla Paranal Observatory under programme ID 072.C-0488. This research has made use of the SIMBAD and VizieR services, both operated at Centre de Données astronomiques de Strasbourg (CDS; <https://cds.u-strasbg.fr/>) in France, and NASA’s Astrophysics Data System Bibliographic Services. This research made use of Lightkurve, a Python package for Kepler and TESS data analysis (Lightkurve Collaboration et al. 2018). We used TESSCut (Brasseur et al. 2019) in the analysis that was based on TRICERATOPS (Giacalone & Dressing 2020). This publication makes use of data products from the Two Micron All Sky Survey (Skrutskie et al. 2003), which is a joint project of the University of Massachusetts and the Infrared Processing and Analysis Center/California Institute of Technology, funded by the National Aeronautics and Space Administration and the National Science Foundation. This research has made use of the NASA Exoplanet Archive (DOI:[10.26133/NEA12](https://doi.org/10.26133/NEA12)), which is operated by the California Institute of Technology, under contract with the National Aeronautics and Space Administration under the Exoplanet Exploration Program. IRAF, which we used in reducing IRD raw data, is distributed by the National Optical Astronomy Observatories, which is operated by the Association of Universities for Research in Astronomy, Inc. (AURA) under cooperative agreement with the National Science Foundation. This research has made use of the Exoplanet Follow-up Observation Program (ExoFOP; DOI:[10.26134/ExoFOP5](https://doi.org/10.26134/ExoFOP5)) website, which is operated by the California Institute of Technology, under contract with the National Aeronautics and Space Administration under the Exoplanet Exploration Program. Part of the data analysis was carried out on the Multi-wavelength Data Analysis System operated by the Astronomy Data Center (ADC), National Astronomical Observatory of Japan. Part of this work was carried out at the Jet Propulsion Laboratory, California Institute of Technology, under contract with NASA.

We are honored and grateful for the opportunity of observing the Universe from Maunakea, which has cultural, historical, and natural significance in Hawaii. We appreciate the critical support from all the current and recent Subaru and Keck

Observatory staffs. Their support was essential in achieving this discovery, especially amidst the many difficulties associated with the COVID-19 pandemic.

This research is based on data collected at the Subaru Telescope, which is operated by the National Astronomical Observatory of Japan. This Letter is based on observations made with the MuSCAT2 instrument, developed by ABC, at Telescopio Carlos Sánchez, operated on the island of Tenerife by the IAC in the Spanish Observatorio del Teide. This Letter is based on observations made with the MuSCAT3 instrument, developed by the Astrobiology Center and under financial support by JSPS KAKENHI (JP18H05439) and JST PRESTO (JPMJPR1775), at Faulkes Telescope North on Maui, Hawaii, operated by the Las Cumbres Observatory. CARMENES is an instrument at the Centro Astronómico Hispano en Andalucía (CAHA) at Calar Alto (Almería, Spain), operated jointly by the Junta de Andalucía and the Instituto de Astrofísica de Andalucía (CSIC). Some of the data presented herein were obtained at the W. M. Keck Observatory, which is operated as a scientific partnership among the California Institute of Technology, the University of California, and the National Aeronautics and Space Administration. The Observatory was made possible by the generous financial support of the W. M. Keck Foundation.

M.T. is supported by JSPS KAKENHI grant Nos. 18H05442, 15H02063, and 22000005. This work is partly supported by JSPS KAKENHI grant Nos. JP18H05439, JP21K13955, and JP21K20376 and JST CREST grant No. JPMJCR1761. M.O. is funded by the National Natural Science Foundation of China (Nos. 12250610186, 12273023). We acknowledge financial support from the Agencia Estatal de Investigación (AEI/10.13039/501100011033) of the Ministerio de Ciencia e Innovación and the ERDF “A way of making Europe” through projects PID2021-125627OB-C31, PID2021-125627OB-C32, and PID2019-109522GB-C5[1:4]; the grant PRE2020-093107 of the Pre-Doc Program for the Training of Doctors (FPI-SO) through FSE funds; and the Centre of Excellence “Severo Ochoa” and “María de Maeztu” awards to the Instituto de Astrofísica de Canarias (CEX2019-000920-S) and Institut de Ciències de l’Espai (CEX2020-001058-M). K. A.C. acknowledges support from the TESS mission via subaward s3449 from MIT. D.R. was supported by NASA under award No. NNA16BD14C for NASA Academic Mission Services. R.L. acknowledges funding from the University of La Laguna through the Margarita Salas Fellowship from the Spanish Ministry of Universities ref. UNI/551/2021-May 26 and under the EU Next Generation funds. M.S. acknowledges the support of the Italian National Institute of Astrophysics (INAF) through the project “The HOT-ATMOS Project: characterizing the atmospheres of hot giant planets as a key to understand the exoplanet diversity” (1.05.01.85.04). G. M. acknowledges funding from the Ariel Postdoctoral Fellowship program of the Swedish National Space Agency (SNSA). J.K. gratefully acknowledges the support of the Swedish Research Council (VR: Etableringsbidrag 2017-04945). We acknowledge the support from the Deutsche Forschungsgemeinschaft (DFG) under Research Unit FOR2544 “Blue Planets around Red Stars” through project DR 281/32-1. The results reported herein benefited from collaborations and/or information exchange within NASA’s Nexus for Exoplanet System Science (NExSS) research coordination network sponsored by NASA’s Science Mission Directorate under

agreement No. 80NSSC21K0593 for the program “Alien Earths.” Part of this work was also supported by NAOJ Research Coordination Committee, NINS, NAOJ-RCC2301-0401.

Facilities: TESS, Keck:II (NIRC2), Gemini-North (Altair, NIRI), the 1.52 m Telescopio Carlos Sánchez (MuSCAT2), the 2 m Faulkes Telescope North (MuSCAT3), the Subaru Telescope (IRD), the 3.5 m Calar Alto telescope (CARMENES), XMN-Newton, the ESO La Silla 3.6 m telescope (HARPS), SuperWASP, ASAS-SN, MEearth, Exoplanet Archive.

Software: `astropy` (Astropy Collaboration et al. 2013, 2018, 2022), `PyAstronomy` (Czesla et al. 2019; <https://github.com/sczesla/PyAstronomy>), `corner` (Foreman-Mackey 2016), `celerite` (Foreman-Mackey et al. 2017), `emcee` (Foreman-Mackey et al. 2013), `GGChem` (Woitke & Helling 2021), `IRAF` (Tody 1986, 1993), `IRD RV-measurement pipeline` (Hirano et al. 2020), `lighkurve` (Lightkurve Collaboration et al. 2018), `LDTk` (Parviainen & Aigrain 2015), `matplotlib` (Hunter 2007), `nirlyn` (<https://www.gemini.edu/instrumentation/niri/data-reduction>), `numpy` (van der Walt et al. 2011), `Pandexo` (Batalha et al. 2017), `PyTransit` (Parviainen 2015), `scipy` (Virtanen et al. 2020), `serval` (Zechmeister et al. 2018), `SteParSyn` (Tabernero et al. 2022), `TauREx3` (Al-Refaie et al. 2021), `TESSCut` (Brasseur et al. 2019), `TRICERATOPS` (Giacalone & Dressing 2020), `pandas` (McKinney 2010), `SymPy` (Meurer et al. 2017), Google Colaboratory.

Appendix A High-contrast Imaging and Data Reduction

A.1. Gemini/NIRI

The near-infrared observations of Gliese 12 were performed with the *f*/32 camera of NIRI and the Altair field lens, which set the plate scale to be 21.4 mas pixel⁻¹. A partial readout mode was employed to image only the central 512 × 512 pixels of the full FoV of the Altair+NIRI combination. The *J*-, *H*-, and *K*-band observations obtained six images with dithering. At each dither position, a single frame was made by integrating five subframes (i.e., five coadds) taken with individual exposures of 0.15 s in *H*- and *K*-band imaging and 1.2 s in *J*-band imaging.

We reduced the archival Gemini/NIRI data with a custom-made script as follows. In the script, we also used a Python program for linearity correction developed by the NIRI instrument team, which is `nirlyn.py` and available from <https://www.gemini.edu/instrumentation/niri/data-reduction>. We performed the raw-data processing in this order: linearity correction, horizontal-stripe pattern subtraction, flat-fielding, sky subtraction, bad-pixel interpolation, distortion correction, and alignment of Gliese 12’s PSF centers. The horizontal-stripe pattern of the detector was removed by subtracting each row of the detector by its median flux after masking out pixels containing flux from the star. Based on communication with NIRI instrument expert A. Stevens, we did not apply `cleanir.py` for subtracting the eight-column noise pattern, since the pattern was not present in the images. The script for linearity correction cannot handle data with image sizes of 512 × 512 pixels. We therefore applied all correction functions that are appropriate for other image sizes to the data and tested whether the output contrast measurements settled into

consistent results regardless of the adopted functions. A total of 99% of the measurements are consistent within 0.05 mag, indicating that there are no significant differences between different nonlinearity corrections. The images were taken with a fixed Cassegrain rotator in order to optimize the AO corrections. In this mode, the field rotates; we therefore derotated the images based on the information in the fits headers to align the FoVs to the north direction. Finally, we combined all the processed images at J , H , and K into three master images at each band (see Figure 3).

A.2. *Keck II/NIRC2+PyWFS*

We obtained two cycles of three K' -band ($\approx 2.12 \mu\text{m}$) images at different dithering positions. Then, each image of the first cycle was obtained by coadding five subimages taken with 1 s exposure, while 10 subimages of 1 s exposure were coadded at each dithering position in the second cycle. We also obtained six images with a narrowband filter corresponding to the $\text{Br}\gamma$ feature ($\approx 2.17 \mu\text{m}$) for aperture corrections. The $\text{Br}\gamma$ images were used as the unsaturated reference PSFs to compensate the saturated cores of PSFs in the photometry of the K' -band images under the assumption that the PSF shapes are quite

similar between K' and $\text{Br}\gamma$. We checked whether the assumption affected the contrast measurements with the unsaturated PSFs of the other two M dwarfs observed in the same night. The measurements are in agreement within 10%, ensuring that the above assumption does not influence our conclusions.

We performed dark subtraction, flat-fielding correction, and bad-pixel removal to calibrate the raw NIRC2 data. We next calibrated the camera's optical distortion with the script provided by Yelda et al. (2010) and the distortion solution from Service et al. (2016), which sets the plate scale to be $9.971 \text{ mas pixel}^{-1}$ in the distortion-corrected image. We combined the calibrated images after shifting the primary star's PSFs to a common position. Before combining the images, we also rotated them to align in the north direction along the y -axis of the images because we conducted the observations with the pupil-tracking mode. Figure 3 shows the combined image.

Appendix B RV Measurements of Gliese 12

Table 3 lists Gliese 12's relative RVs measured with IRD and CARMENES.

Table 3
Relative RV Measurements of Gliese 12

BJD (days)	RV (m s^{-1})	σ_{RV} (m s^{-1})	Instrument
2458657.1081023	7.78	3.68	IRD
2458772.8545807	-6.94	3.57	IRD
2458828.7733195	-2.78	3.89	IRD
2459032.1058368	7.91	3.31	IRD
2459032.1108176	2.5	3.57	IRD
2459091.1383862	-0.69	3.61	IRD
2459091.1444178	-2.78	3.61	IRD
2459091.9128072	5.87	3.07	IRD
2459092.8994228	-1.04	3.31	IRD
2459092.9072207	2.39	3.49	IRD
2459098.9899503	-0.85	3.69	IRD
2459098.9954901	4.91	3.67	IRD
2459107.8986615	-5.44	3.24	IRD
2459107.9064719	-1.58	3.37	IRD
2459108.8313943	1.98	3.26	IRD
2459108.8421331	3.68	3.41	IRD
2459109.8320718	-1.73	3.09	IRD
2459109.8428024	3.87	3.23	IRD
2459110.8857408	-3.09	3.56	IRD
2459110.8964816	-3.19	3.31	IRD
2459111.8681702	-5.44	3.48	IRD
2459111.8812654	4.34	8.06	IRD
2459112.9655217	-1.16	3.43	IRD
2459112.9744962	2.75	3.18	IRD
2459115.0326667	-1.26	3.51	IRD
2459115.0387004	-4.78	3.22	IRD
2459118.0189589	-0.90	3.43	IRD
2459118.0261636	2.70	3.27	IRD
2459123.8158675	-4.08	3.36	IRD
2459123.8236605	0.53	3.31	IRD
2459125.8172895	-1.52	3.00	IRD
2459125.8280198	1.36	3.34	IRD
2459128.8497845	-7.66	3.35	IRD
2459128.8605252	0.60	3.44	IRD
2459153.8646901	0.28	2.98	IRD
2459153.8765642	0.00	2.98	IRD
2459182.8403137	-8.08	3.68	IRD
2459182.8510060	-2.88	3.55	IRD

Table 3
(Continued)

BJD (days)	RV (m s^{-1})	σ_{RV} (m s^{-1})	Instrument
2459454.0011469	13.07	4.28	IRD
2459454.0048046	7.78	4.39	IRD
2459456.1086614	6.86	4.11	IRD
2459456.1140850	9.15	4.34	IRD
2459468.8528721	0.41	3.98	IRD
2459468.8573561	-7.94	3.82	IRD
2459486.8983724	-0.30	3.78	IRD
2459486.9020344	1.73	3.90	IRD
2459508.9949030	4.82	4.05	IRD
2459508.9985653	1.73	4.05	IRD
2459511.9844461	-4.75	4.18	IRD
2459511.9892896	1.00	4.11	IRD
2459513.0088874	-0.08	3.61	IRD
2459513.0149102	0.34	4.01	IRD
2459529.8861489	8.85	3.94	IRD
2459529.8900382	3.60	3.90	IRD
2459854.0161688	6.13	3.82	IRD
2459854.0210022	11.55	4.01	IRD
2459890.8249876	6.15	4.22	IRD
2459890.8286465	-0.19	3.93	IRD
2459891.9583209	-4.19	4.55	IRD
2459891.9631482	-0.87	4.26	IRD
2459892.9638331	5.67	4.04	IRD
2459892.9686761	5.54	4.06	IRD
2459893.9629992	8.26	3.60	IRD
2459893.9706576	8.93	3.65	IRD
2459894.9363576	-1.51	3.86	IRD
2459894.9423608	-4.99	3.97	IRD
2459896.9683733	0.64	3.50	IRD
2459896.9790742	4.49	3.64	IRD
2459897.8840425	-4.65	4.15	IRD
2459897.8877025	2.02	4.29	IRD
2459907.8269676	-1.94	3.61	IRD
2459907.8318053	-5.50	3.97	IRD
2459908.8295062	-6.44	4.11	IRD
2459908.8329353	-3.18	4.48	IRD
2459950.7186219	-4.38	4.14	IRD
2459950.7234543	-3.62	4.31	IRD
2460123.5931062	-0.54	1.69	CARMENES
2460124.5932957	1.84	2.71	CARMENES
2460125.6430641	-0.46	1.27	CARMENES
2460127.6440508	-0.90	1.42	CARMENES
2460133.6110069	-1.38	2.40	CARMENES
2460157.6029270	2.78	1.39	CARMENES
2460158.5175814	0.89	1.96	CARMENES
2460168.6194806	-3.12	1.29	CARMENES
2460170.6250763	-3.13	1.30	CARMENES
2460172.5947363	-1.73	2.01	CARMENES
2460176.6622728	-3.82	1.55	CARMENES
2460180.5947426	0.42	1.48	CARMENES
2460184.5995223	5.11	2.78	CARMENES
2460193.6313475	4.36	2.01	CARMENES
2460195.5738182	5.26	1.86	CARMENES
2460196.5756710	3.25	1.56	CARMENES
2460198.6561354	0.68	1.72	CARMENES

Note. The BJDs, RVs, and RV errors were rounded from the ones originally provided by the pipelines.

Appendix C Odd–Even Transit Plot for the TESS Data

The phase-folded TESS light curves of the odd- and even-numbered transits for the $P = 12.76$ day ephemeris are shown

in Figure 11, which was truncated from the DV report produced by the SPOC pipeline (Twicken et al. 2018) from Sectors 40–70.

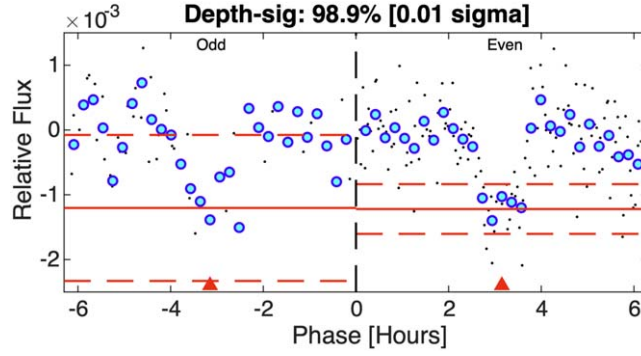


Figure 11. TESS light curves (black dots) of Gliese 12 for the odd- (left) and even-numbered (right) transits. They were phase-folded for the $P = 12.76$ day ephemeris. Binned data points are shown as cyan-filled blue circles. The transit depths and 1σ uncertainties were determined from independent transit model fits to each light curve and are shown as horizontal red solid and dashed lines. The “Depth-sig” at the top of the plot is the statistical significance of the difference between the odd and even transit depths. The low significance (0.01σ) indicates there is no significant discrepancy in the measured depths between the two sets. The plots are reproduced from the DV report produced by the SPOC pipeline (Twicken et al. 2018) for Sectors 40–70 (the full report is available from MAST).

Appendix D

Priors and Posteriors of the Light-curve Analyses

Table 4 summarizes the priors and posteriors of the transit model parameters used for the analyses of light curves obtained with TESS, MuSCAT2, and MuSCAT3 (Sections 4.2.1 and 4.2.2).

Table 4
Priors and Posteriors of the Parameters Adopted in the Transit Modeling for the TESS and MuSCAT Light Curves

Parameter	Unit	Prior ^a	Posterior (TESS)	Posterior (MuSCAT series)
b		$\mathcal{U}(0, 1)$	$0.55^{+0.31}_{-0.37}$	$0.60^{+0.21}_{-0.37}$
$\ln a_R$		$\mathcal{U}(0, 5.3)$	$4.23^{+0.18}_{-0.50}$	$4.25^{+0.19}_{-0.30}$
$k (= R_p/R_s)$		$\mathcal{U}(0, 0.3)$	$0.0320^{+0.0032}_{-0.0021}$	$0.0326^{+0.0025}_{-0.0019}$
$T_{c,0}$	BJD	$\mathcal{U}(0, \infty)$	2459497.1848 ± 0.0036	$2459497.1842^{+0.0086}_{-0.0082}$
P	days	$\mathcal{U}(11.5, 14.0)$	$12.76146^{+0.00009}_{-0.00011}$	12.76145 ± 0.00016
$u_{1,TESS}$		$\mathcal{N}(0.261, 0.004)$	0.261 ± 0.004	...
$u_{2,TESS}$		$\mathcal{N}(0.308, 0.008)$	0.309 ± 0.008	...
$u_{1,r}$		$\mathcal{N}(0.458, 0.011)$...	0.458 ± 0.011
$u_{2,r}$		$\mathcal{N}(0.354, 0.017)$...	0.353 ± 0.017
$u_{1,i}$		$\mathcal{N}(0.285, 0.006)$...	0.285 ± 0.006
$u_{2,i}$		$\mathcal{N}(0.351, 0.011)$...	0.350 ± 0.011
u_{1,z_s}		$\mathcal{N}(0.222, 0.005)$...	0.222 ± 0.005
u_{2,z_s}		$\mathcal{N}(0.320, 0.010)$...	0.320 ± 0.010

Note.

^a $\mathcal{U}(a, b)$ denotes a uniform distribution between a and b , and $\mathcal{N}(a, b)$ denotes a normal distribution with the mean of a and variance of b^2 .

Appendix E Posteriors of the Joint-fit Parameters

Figure 12 shows a corner plot for the posterior probability distributions of selected transit+RV parameters calculated

from the joint MCMC analysis in Section 4.5. Figure 13 shows the individual midtransit times derived from the same analysis, where the best-fit linear ephemeris is subtracted.

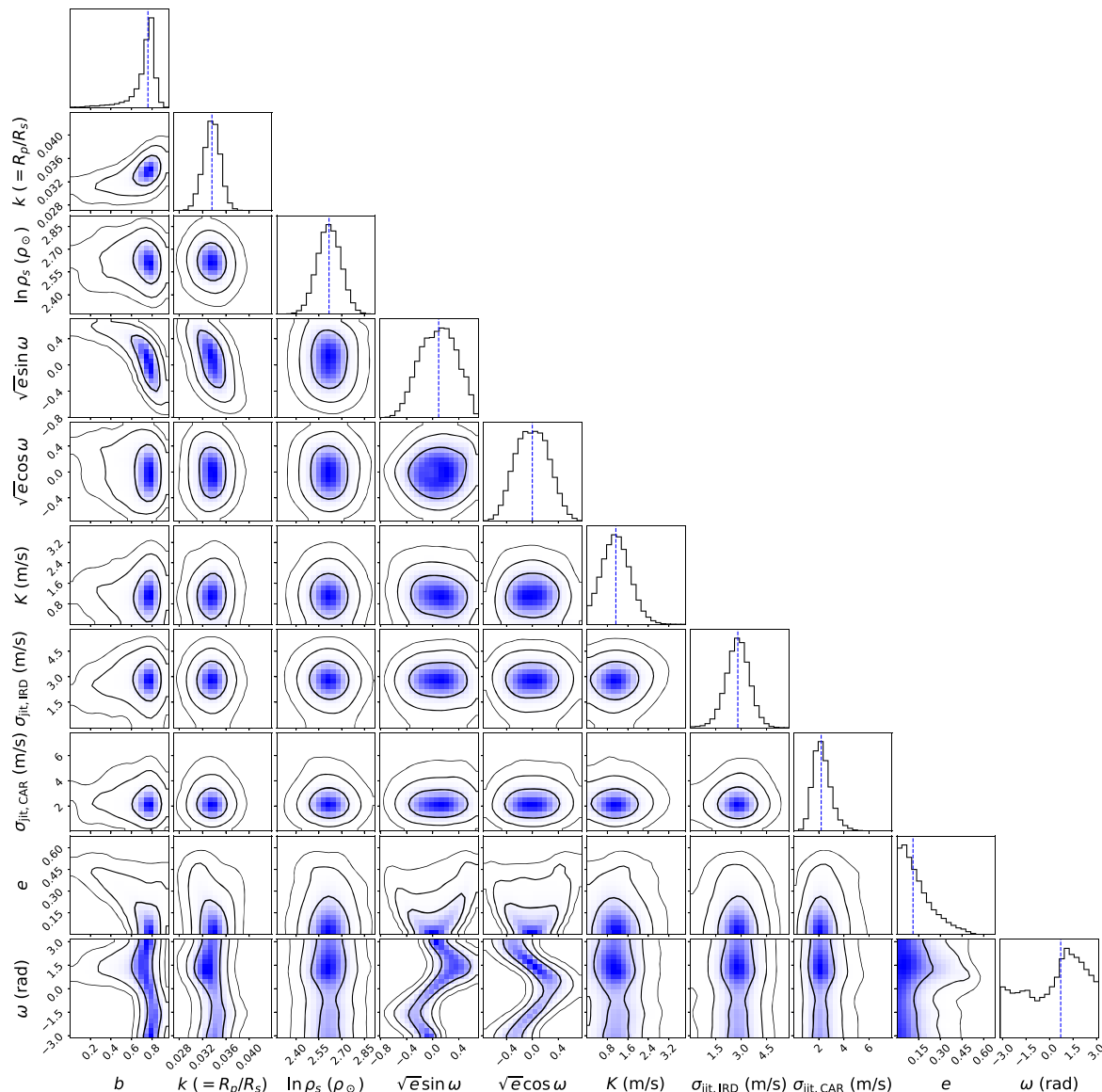


Figure 12. Corner plot for the posteriors of the joint-fit parameters calculated from the joint MCMC analysis. The probability density is shown in blue, while 1σ , 2σ , and 3σ confidence intervals are shown in the thickest, second-thickest, and thinnest black lines, respectively. The median value of each parameter is indicated by the vertical dashed line in the histograms.

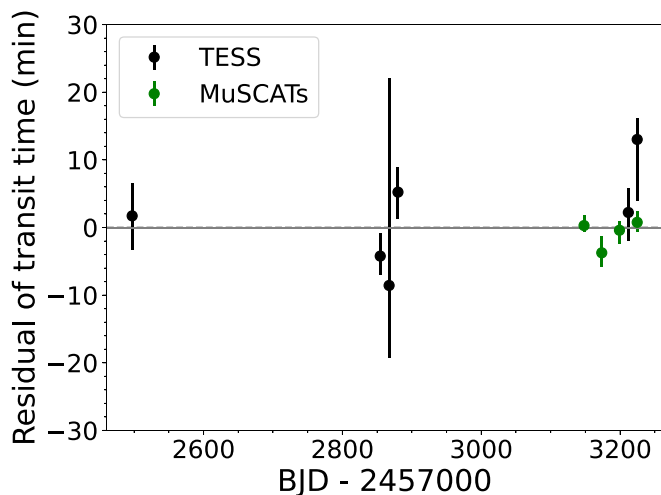


Figure 13. Midtransit times of Gliese 12 b measured in the TESS (black) and MuSCAT series (green) data with the best-fit linear ephemeris subtracted, showing no significant TTVs. Note that the measurement with large error bars (the third data point from TESS) comes from a partial transit (transit epoch = 29).

ORCID iDs

Masayuki Kuzuhara <https://orcid.org/0000-0002-4677-9182>

Akihiko Fukui <https://orcid.org/0000-0002-4909-5763>

John H. Livingston <https://orcid.org/0000-0002-4881-3620>

José A. Caballero <https://orcid.org/0000-0002-7349-1387>

Jerome P. de Leon <https://orcid.org/0000-0002-6424-3410>

Teruyuki Hirano <https://orcid.org/0000-0003-3618-7535>

Yui Kasagi <https://orcid.org/0000-0002-8607-358X>

Felipe Murgas <https://orcid.org/0000-0001-9087-1245>

Norio Narita <https://orcid.org/0000-0001-8511-2981>

Masashi Omiya <https://orcid.org/0000-0002-5051-6027>

Jaume Orell-Miquel <https://orcid.org/0000-0003-2066-8959>

Enric Palle <https://orcid.org/0000-0003-0987-1593>

Quentin Changeat <https://orcid.org/0000-0001-6516-4493>

Emma Esparza-Borges <https://orcid.org/0000-0002-2341-3233>

Hiroki Harakawa <https://orcid.org/0000-0002-7972-0216>

Coel Hellier <https://orcid.org/0000-0002-3439-1439>

Yasunori Hori <https://orcid.org/0000-0003-4676-0251>

Kai Ikuta <https://orcid.org/0000-0002-5978-057X>

Hiroyuki Tako Ishikawa <https://orcid.org/0000-0001-6309-4380>

Takanori Kodama <https://orcid.org/0000-0001-9032-5826>

Takayuki Kotani <https://orcid.org/0000-0001-6181-3142>

Tomoyuki Kudo <https://orcid.org/0000-0002-9294-1793>

Juan C. Morales <https://orcid.org/0000-0003-0061-518X>

Mayuko Mori <https://orcid.org/0000-0003-1368-6593>

Evangelos Nagel <https://orcid.org/0000-0002-4019-3631>

Hannu Parviainen <https://orcid.org/0000-0001-5519-1391>

Volker Perdelwitz <https://orcid.org/0000-0002-6859-0882>

Ansgar Reiners <https://orcid.org/0000-0003-1242-5922>

Ignasi Ribas <https://orcid.org/0000-0002-6689-0312>

Jorge Sanz-Forcada <https://orcid.org/0000-0002-1600-7835>

Bun'ei Sato <https://orcid.org/0000-0001-8033-5633>

Andreas Schweitzer <https://orcid.org/0000-0002-1624-0389>

Hugo M. Taberner <https://orcid.org/0000-0002-8087-4298>

Takuya Takarada <https://orcid.org/0009-0006-9082-9171>

Taichi Uyama <https://orcid.org/0000-0002-6879-3030>

Noriharu Watanabe <https://orcid.org/0000-0002-7522-8195>

Mathias Zechmeister <https://orcid.org/0000-0002-6532-4378>

Néstor Abreu García <https://orcid.org/0009-0002-5067-5463>

Wako Aoki <https://orcid.org/0000-0002-8975-6829>

Charles Beichman <https://orcid.org/0000-0002-5627-5471>

Víctor J. S. Béjar <https://orcid.org/0000-0002-5086-4232>

Timothy D. Brandt <https://orcid.org/0000-0003-2630-8073>

Ilaria Carleo <https://orcid.org/0000-0002-0810-3747>

David Charbonneau <https://orcid.org/0000-0002-9003-484X>

Karen A. Collins <https://orcid.org/0000-0001-6588-9574>

Thayne Currie <https://orcid.org/0000-0002-7405-3119>

Stefan Dreizler <https://orcid.org/0000-0001-6187-5941>

Gareb Fernández-Rodríguez <https://orcid.org/0000-0003-0597-7809>

Izuru Fukuda <https://orcid.org/0000-0002-9436-2891>

Daniel Galán <https://orcid.org/0000-0001-6191-8251>

Yuya Hayashi <https://orcid.org/0000-0001-8877-0242>

Christina Hedges <https://orcid.org/0000-0002-3385-8391>

Thomas Henning <https://orcid.org/0000-0002-1493-300X>

Masahiro Ikoma <https://orcid.org/0000-0002-5658-5971>

Keisuke Isogai <https://orcid.org/0000-0002-6480-3799>

Markus Janson <https://orcid.org/0000-0001-8345-593X>

Jon M. Jenkins <https://orcid.org/0000-0002-4715-9460>

Taiki Kageyama <https://orcid.org/0000-0002-5331-6637>

Yugo Kawai <https://orcid.org/0000-0002-0488-6297>

Kiyoe Kawachi <https://orcid.org/0000-0003-1205-5108>

Eiichiro Kokubo <https://orcid.org/0000-0002-5486-7828>

Mihoko Konishi <https://orcid.org/0000-0003-0114-0542>

Judith Korth <https://orcid.org/0000-0002-0076-6239>

Vigneshwaran Krishnamurthy <https://orcid.org/0000-0003-2310-9415>

Nobuhiko Kusakabe <https://orcid.org/0000-0001-9194-1268>

Andrés Laza-Ramos <https://orcid.org/0000-0003-3316-3044>

Rafael Luque <https://orcid.org/0000-0002-4671-2957>

Alberto Madrigal-Aguado <https://orcid.org/0000-0002-9510-0893>

Yuji Matsumoto <https://orcid.org/0000-0002-2383-1216>

Dimitri Mawet <https://orcid.org/0000-0002-8895-4735>

Michael W. McElwain <https://orcid.org/0000-0003-0241-8956>

Pedro Pablo Meni Gallardo <https://orcid.org/0009-0001-7943-0075>

Giuseppe Morello <https://orcid.org/0000-0002-4262-5661>

Sara Muñoz Torres <https://orcid.org/0000-0003-4269-4779>

Jun Nishikawa <https://orcid.org/0000-0001-9326-8134>

Stevanus K. Nugroho <https://orcid.org/0000-0003-4698-6285>

Masahiro Ogihara <https://orcid.org/0000-0002-8300-7990>

Alberto Peláez-Torres <https://orcid.org/0000-0001-9204-8498>



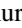



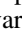

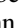
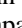
David Rapetti <https://orcid.org/0000-0003-2196-6675>

Manuel Sánchez-Benavente <https://orcid.org/0000-0003-2693-279X>

Martin Schlecker <https://orcid.org/0000-0001-8355-2107>

Sara Seager <https://orcid.org/0000-0002-6892-6948>

Monika Stangret <https://orcid.org/0000-0002-1812-8024>

Aoi Takahashi  <https://orcid.org/0000-0003-3881-3202>
 Huan-Yu Teng  <https://orcid.org/0000-0003-3860-6297>
 Motohide Tamura  <https://orcid.org/0000-0002-6510-0681>
 Yuka Terada  <https://orcid.org/0000-0003-2887-6381>
 Tomonori Usuda  <https://orcid.org/0000-0001-9855-0163>
 Roland Vanderspek  <https://orcid.org/0000-0001-6763-6562>
 Sébastien Vievard  <https://orcid.org/0000-0003-4018-2569>
 David Watanabe  <https://orcid.org/0000-0002-3555-8464>
 Joshua N. Winn  <https://orcid.org/0000-0002-4265-047X>
 Maria Rosa Zapatero Osorio  <https://orcid.org/0000-0001-5664-2852>

References

- Agol, E., Dorn, C., Grimm, S. L., et al. 2021, *PSJ*, **2**, 1
 Allard, F. 2014, in IAU Symp. 299, Exploring the Formation and Evolution of Planetary Systems, ed. M. Booth, B. C. Matthews, & J. R. Graham, 299 (Cambridge: Cambridge Univ. Press), 271
 Al-Refaie, A. F., Changeat, Q., Waldmann, I. P., & Tinetti, G. 2021, *ApJ*, **917**, 37
 Astropy Collaboration, Price-Whelan, A. M., Lim, P. L., et al. 2022, *ApJ*, **935**, 167
 Astropy Collaboration, Price-Whelan, A. M., Sipőcz, B. M., et al. 2018, *AJ*, **156**, 123
 Astropy Collaboration, Robitaille, T. P., Tollerud, E. J., et al. 2013, *A&A*, **558**, A33
 Astudillo-Defru, N., Delfosse, X., Bonfils, X., et al. 2017, *A&A*, **600**, A13
 Barros, S. C. C., Demangeon, O. D. S., Alibert, Y., et al. 2022, *A&A*, **665**, A154
 Batalha, N. E., Mandell, A., Pontoppidan, K., et al. 2017, *PASP*, **129**, 064501
 Becker, J., Gallo, E., Hodges-Kluck, E., Adams, F. C., & Barnes, R. 2020, *AJ*, **159**, 275
 Belokurov, V., Penoyre, Z., Oh, S., et al. 2020, *MNRAS*, **496**, 1922
 Baluev, R. V. 2008, *MNRAS*, **385**, 1279
 Bensby, T., Feltzing, S., & Oey, M. S. 2014, *A&A*, **562**, A71
 Berta, Z. K., Irwin, J., Charbonneau, D., Burke, C. J., & Falco, E. E. 2012, *AJ*, **144**, 145
 Bond, C. Z., Cetre, S., Lilley, S., et al. 2020, *JATIS*, **6**, 039003
 Bonfils, X., Lo Curto, G., Correia, A. C. M., et al. 2013, *A&A*, **556**, A110
 Bouma, L. G., Hartman, J. D., Brahm, R., et al. 2020, *AJ*, **160**, 239
 Brasseur, C. E., Phillip, C., Fleming, S. W., Mullally, S. E., & White, R. L., 2019 Astrocut: Tools for Creating Cutouts of TESS Images, Astrophysics Source Code Library, ascl:1905.007
 Burdanov, A. Y., Lederer, S. M., Gillon, M., et al. 2019, *MNRAS*, **487**, 1634
 Caramazza, M., Stelzer, B., Magaúda, E., et al. 2023, *A&A*, **676**, A14
 Charbonneau, D., Irwin, J., Nutzman, P., & Falco, E. E. 2008, AAS Meeting Abstracts, **212**, 44.02
 Chen, J., & Kipping, D. 2017, *ApJ*, **834**, 17
 Chubb, K. L., Tennyson, J., & Yurchenko, S. N. 2020, *MNRAS*, **493**, 1531
 Crossfield, I. J. M., Malik, M., Hill, M. L., et al. 2022, *ApJL*, **937**, L17
 Czesla, S., Schröter, S., Schneider, P., C., et al., 2019 PyA: Python astronomy-related packages, Astrophysics Source Code Library, ascl:1906.010
 de Wit, J., Wakeford, H. R., Gillon, M., et al. 2016, *Natur*, **537**, 69
 de Wit, J., Wakeford, H. R., Lewis, N. K., et al. 2018, *NatAs*, **2**, 214
 Delrez, L., Gillon, M., Queloz, D., et al. 2018, *Proc. SPIE*, **10700**, 1070011
 Delrez, L., Murray, C. A., Josse, F. J., et al. 2022, *A&A*, **667**, A59
 Foreman-Mackey, D. 2016, *MOAG*, **1**, 24
 Foreman-Mackey, D., Agol, E., Ambikasaran, S., & Angus, R. 2017, *AJ*, **154**, 220
 Foreman-Mackey, D., Hogg, D. W., Lang, D., & Goodman, J. 2013, *PASP*, **125**, 306
 Fuhrmann, K., Chini, R., Kaderhandt, L., & Chen, Z. 2017, *MNRAS*, **464**, 2610
 Fukui, A., Narita, N., Tristram, P. J., et al. 2011, *PASJ*, **63**, 287
 Gaia Collaboration, Brown, A. G. A., Vallenari, A., et al. 2018, *A&A*, **616**, A1
 Gaia Collaboration, Prusti, T., de Bruijne, J. H. J., et al. 2016, *A&A*, **595**, A1
 Gaia Collaboration, Vallenari, A., Brown, A. G. A., et al. 2023, *A&A*, **674**, A1
 Garcia-Piquer, A., Morales, J. C., Ribas, I., et al. 2017, *A&A*, **604**, A87
 Gialalone, S., & Dressing, C. D., 2020 triceratops: Candidate exoplanet rating tool, Astrophysics Source Code Library, ascl:2002.004
 Gialalone, S., Dressing, C. D., Jensen, E. L. N., et al. 2021, *AJ*, **161**, 24
 Gilbert, E. A., Vanderburg, A., Rodriguez, J. E., et al. 2023, *ApJL*, **944**, L35
 Gillon, M., Triaud, A. H. M. J., Demory, B.-O., et al. 2017, *Natur*, **542**, 456
 Gorrini, P., Kemmer, J., Dreizler, S., et al. 2023, *A&A*, **680**, A28
 Greene, T. P., Bell, T. J., Ducrot, E., et al. 2023, *Natur*, **618**, 39
 Gressier, A., Mori, M., Changeat, Q., et al. 2022, *A&A*, **658**, A133
 Guerrero, N. M., Seager, S., Huang, C. X., et al. 2021, *ApJS*, **254**, 39
 Haldemann, J., Alibert, Y., Mordasini, C., & Benz, W. 2020, *A&A*, **643**, A105
 Harakawa, H., Takarada, T., Kasagi, Y., et al. 2022, *PASJ*, **74**, 904
 Herriot, G., Morris, S., Anthony, A., et al. 2000, *Proc. SPIE*, **4007**, 115
 Hirano, T., Dai, F., Livingston, J. H., et al. 2023, *AJ*, **165**, 131
 Hirano, T., Kuzuhara, M., Kotani, T., et al. 2020, *PASJ*, **72**, 93
 Hodapp, K. W., Jensen, J. B., Irwin, E. M., et al. 2003, *PASP*, **115**, 1388
 Houdebine, E. R., Mullan, D. J., Paletou, F., & Gebran, M. 2016, *ApJ*, **822**, 97
 Howard, W. S., Kowalski, A. F., Flagg, L., et al. 2023, *ApJ*, **959**, 64
 Howell, S. B., Sobeck, C., Haas, M., et al. 2014, *PASP*, **126**, 398
 Hunter, J. D. 2007, *CSE*, **9**, 90
 Ishikawa, H. T., Aoki, W., Hirano, T., et al. 2022, *AJ*, **163**, 72
 Ishikawa, H. T., Aoki, W., Kotani, T., et al. 2020, *PASJ*, **72**, 102
 Jakobsen, P., Ferruit, P., Alves de Oliveira, C., et al. 2022, *A&A*, **661**, A80
 Jansen, F., Lumb, D., Altieri, B., et al. 2001, *A&A*, **365**, L1
 Jenkins, J. M. 2002, *ApJ*, **575**, 493
 Jenkins, J. M., Tenenbaum, P., Seader, S., et al. 2020, Kepler Data Processing Handbook: Transiting Planet Search, Kepler Science Document KSCI-19081-003
 Jenkins, J. M., Twicken, J. D., McCauliff, S., et al. 2016, *Proc. SPIE*, **9913**, 99133E
 Johnstone, C. P., Bartel, M., & Güdel, M. 2021, *A&A*, **649**, A96
 Jurić, M., Ivezić, Ž., Brooks, A., et al. 2008, *ApJ*, **673**, 864
 Kempton, E. M. R., Bean, J. L., Louie, D. R., et al. 2018, *PASP*, **130**, 114401
 Kiman, R., Faherty, J. K., Cruz, K. L., et al. 2021, *AJ*, **161**, 277
 Kipping, D. M. 2014, *MNRAS*, **444**, 2263
 Kochanek, C. S., Shappee, B. J., Stanek, K. Z., et al. 2017, *PASP*, **129**, 104502
 Kodama, T., Genda, H., Oishi, R., Abe-Ouchi, A., & Abe, Y. 2019, *JGRE*, **124**, 2306
 Kopparapu, R. k., Wolf, E. T., Arney, G., et al. 2017, *ApJ*, **845**, 5
 Kotani, T., Tamura, M., Nishikawa, J., et al. 2018, *Proc. SPIE*, **10702**, 1070211
 Kreidberg, L., Koll, D. D. B., Morley, C., et al. 2019, *Natur*, **573**, 87
 Kuzuhara, M., Hirano, T., Kotani, T., et al. 2018, *Proc. SPIE*, **10702**, 1070260
 Li, J., Tenenbaum, P., Twicken, J. D., et al. 2019, *PASP*, **131**, 024506
 Lightkurve Collaboration, Cardoso, J. V. D. M., Hedges, C., et al., 2018 Lightkurve: Kepler and TESS Time Series Analysis in Python, Astrophysics Source Code Library, ascl:1812.013
 Lincowski, A. P., Meadows, V. S., Zieba, S., et al. 2023, *ApJL*, **955**, L7
 Louie, D. R., Deming, D., Albert, L., et al. 2018, *PASP*, **130**, 044401
 Mahadevan, S., Ramsey, L. W., Terrien, R., et al. 2014, *Proc. SPIE*, **9147**, 91471G
 Mainzer, A., Bauer, J., Grav, T., et al. 2011, *ApJ*, **731**, 53
 Maldonado, J., Micela, G., Baratella, M., et al. 2020, *A&A*, **644**, A68
 Mann, A. W., Dupuy, T., Kraus, A. L., et al. 2019, *ApJ*, **871**, 63
 Mayor, M., Pepe, F., Queloz, D., et al. 2003, *Msngr*, **114**, 20
 McKinney, W. 2010, in Proc. of the 9th Python in Science Conf., Data Structures for Statistical Computing in Python, ed. S. van der Walt & J. Millman, 56
 Meurer, A., Smith, C. P., Paprocki, M., et al. 2017, e103, SymPy: symbolic computing in Python, PeerJ Computer Science, 3:e103, doi:10.7717/peerj-cs.103
 McMillan, P. J. 2017, *MNRAS*, **465**, 76
 Mori, M., Livingston, J. H., Leon, J. D., et al. 2022, *AJ*, **163**, 298
 Murgas, F., Castro-González, A., Pallé, E., et al. 2023, *A&A*, **677**, A182
 Nagel, E., Czesla, S., Kaminski, A., et al. 2023, *A&A*, **680**, A73
 Narita, N., Fukui, A., Kusakabe, N., et al. 2019, *JATIS*, **5**, 015001
 Narita, N., Fukui, A., Yamamuro, T., et al. 2020, *Proc. SPIE*, **11447**, 114475K
 NASA Exoplanet Archive 2023a, Planetary Systems, Version: 2023-10-23 07:08, NExSci-Caltech/IPAC, doi:10.26133/NEA12
 NASA Exoplanet Archive 2023b, Planetary Systems, Version: 2023-11-23 09:06, NExSci-Caltech/IPAC, doi:10.26133/NEA12
 Newton, E. R., Charbonneau, D., Irwin, J., et al. 2014, *AJ*, **147**, 20
 Newton, E. R., Irwin, J., Charbonneau, D., et al. 2017, *ApJ*, **834**, 85
 Paegert, M., Stassun, K. G., Collins, K. A., et al. 2021, arXiv.2108.04778
 Parviainen, H. 2015, *MNRAS*, **450**, 3233
 Parviainen, H., & Aigrain, S. 2015, *MNRAS*, **453**, 3821
 Pecaut, M. J., & Mamajek, E. E. 2013, *ApJS*, **208**, 9
 Penz, T., & Micela, G. 2008, *A&A*, **479**, 579
 Perdelwitz, V., Mittag, M., Tal-Or, L., et al. 2021, *A&A*, **652**, A116
 Pollacco, D. L., Skillen, I., Collier Cameron, A., et al. 2006, *PASP*, **118**, 1407
 Polyansky, O. L., Kyuberis, A. A., Zbov, N. F., et al. 2018, *MNRAS*, **480**, 2597
 Quirrenbach, A., Amado, P. J., Caballero, J. A., et al. 2014, *Proc. SPIE*, **9147**, 91471F
 Reid, I. N., Brewer, C., Brucato, R. J., et al. 1991, *PASP*, **103**, 661

- Reid, I. N., Hawley, S. L., & Gizis, J. E. 1995, *AJ*, **110**, 1838
- Reiners, A., Zechmeister, M., Caballero, J. A., et al. 2018, *A&A*, **612**, A49
- Ribas, I., Reiners, A., Zechmeister, M., et al. 2023, *A&A*, **670**, A139
- Ricker, G. R., Winn, J. N., Vanderpek, R., et al. 2015, *JATIS*, **1**, 014003
- Sagear, S., & Ballard, S. 2023, *PNAS*, **120**, e2217398120
- Santerne, A., Díaz, R. F., Almenara, J. M., et al. 2015, *MNRAS*, **451**, 2337
- Sanz-Forcada, J., Micela, G., Ribas, I., et al. 2011, *A&A*, **532**, A6
- Schönrich, R., Binney, J., & Dehnen, W. 2010, *MNRAS*, **403**, 1829
- Seager, S., Kuchner, M., Hier-Majumder, C. A., & Militzer, B. 2007, *ApJ*, **669**, 1279
- Service, M., Lu, J. R., Campbell, R., et al. 2016, *PASP*, **128**, 095004
- Shapsee, B. J., Prieto, J. L., Grupe, D., et al. 2014, *ApJ*, **788**, 48
- Skrutskie, M. F., Cutri, R. M., Stiening, R., et al. 2006, *AJ*, **131**, 1163
- Skrutskie, M. F., Cutri, R. M., Stiening, R., et al. 2003, 2MASS All-Sky Point Source Catalog, IPAC, doi:10.26131/IRSA2
- Smith, J. C., Stumpe, M. C., Van Cleve, J. E., et al. 2012, *PASP*, **124**, 1000
- Soubiran, C., Jasniewicz, G., Chemin, L., et al. 2018, *A&A*, **616**, A7
- Stassun, K. G., Oelkers, R. J., Pepper, J., et al. 2018, *AJ*, **156**, 102
- Strüder, L., Briel, U., Dennerl, K., et al. 2001, *A&A*, **365**, L18
- Stumpe, M. C., Smith, J. C., Catanzarite, J. H., et al. 2014, *PASP*, **126**, 100
- Stumpe, M. C., Smith, J. C., Van Cleve, J. E., et al. 2012, *PASP*, **124**, 985
- Taberner, H. M., Marfil, E., Montes, D., & González Hernández, J. I. 2022, *A&A*, **657**, A66
- Teixeira, K. E., Morley, C. V., Foley, B. J., & Unterborn, C. T. 2024, *ApJ*, **960**, 44
- Tody, D. 1986, *Proc. SPIE*, **627**, 733
- Tody, D. 1993, in ASP Conf. Ser. 52, *Astronomical Data Analysis Software and Systems II*, ed. R. J. Hanisch, R. J. V. Brissenden, & J. Barnes (San Francisco, CA: ASP), 173
- TRAPPIST-1 JWST Community Initiative, de Wit, J., Doyon, R., et al. 2023, arXiv:2310.15895
- Triaud, A. H. M. J., de Wit, J., Klein, F., et al. 2024, *NatAs*, **8**, 17
- Turner, M. J. L., Reeves, J. N., Ponman, T. J., et al. 2001, *A&A*, **365**, L110
- Twicken, J. D., Catanzarite, J. H., Clarke, B. D., et al. 2018, *PASP*, **130**, 064502
- Uyama, T., Beichman, C., Kuzuhara, M., et al. 2023, *AJ*, **165**, 162
- van der Walt, S., Colbert, S. C., & Varoquaux, G. 2011, *CSE*, **13**, 22
- Virtanen, P., Gommers, R., Oliphant, T. E., et al. 2020, *NatMe*, **17**, 261
- Wheatley, P. J., Loudon, T., Bourrier, V., Ehrenreich, D., & Gillon, M. 2017, *MNRAS*, **465**, L74
- Woitke, P., & Helling, C., 2021 GGchem: Fast Thermo-chemical Equilibrium Code, Astrophysics Source Code Library, ascl:2104.018
- Wright, E. L., Eisenhardt, P. R. M., Mainzer, A. K., et al. 2010, *AJ*, **140**, 1868
- Yelda, S., Lu, J. R., Ghez, A. M., et al. 2010, *ApJ*, **725**, 331
- Yurchenko, S. N., Amundsen, D. S., Tennyson, J., & Waldmann, I. P. 2017, *A&A*, **605**, A95
- Yurchenko, S. N., Mellor, T. M., Freedman, R. S., & Tennyson, J. 2020, *MNRAS*, **496**, 5282
- Zechmeister, M., & Kürster, M. 2009, *A&A*, **496**, 577
- Zechmeister, M., Reiners, A., Amado, P. J., et al. 2018, *A&A*, **609**, A12
- Zeng, L., & Sasselov, D. 2013, *PASP*, **125**, 227
- Zieba, S., Kreidberg, L., Ducrot, E., et al. 2023, *Natur*, **620**, 746